

Metagenomic covariation along densely sampled environmental gradients in the Red Sea

Luke R. Thompson^{1,2*}, Gareth J. Williams^{3,4}, Mohamed F. Haroon¹, Ahmed Shibl¹,
Peter Larsen⁵, Joshua Shorenstein², Rob Knight^{2,6}, and Ulrich Stingl^{1*}

¹Red Sea Research Center, King Abdullah University of Science and Technology (KAUST), Thuwal 23955-6900, Saudi Arabia.

²Department of Pediatrics, University of California, San Diego, CA 92037.

³Center for Marine Biodiversity and Conservation, Scripps Institution of Oceanography, La Jolla, CA 92083, USA.

⁴School of Ocean Sciences, Bangor University, Anglesey, LL59 5AB, UK.

⁵Argonne National Laboratory, Argonne, IL 60439.

⁶Department of Computer Science, University of California, San Diego, CA 92037.

*Correspondence to: luket@alum.mit.edu, ulistingl@gmail.com

Running title: Red Sea metagenomic spatial series

Alternate title: A high-resolution spatial map of Red Sea metagenomic diversity

Abstract

Oceanic microbial diversity covaries with physicochemical parameters. Temperature, for example, explains approximately half of global variation in surface taxonomic abundance. It is unknown, however, whether covariation patterns hold over narrower parameter gradients and spatial scales, and extending to mesopelagic depths. We collected and sequenced 45 epipelagic and mesopelagic microbial metagenomes on a meridional transect through the eastern Red Sea. We asked which environmental parameters explain the most variation in relative abundances of taxonomic groups, gene ortholog groups, and pathways—at a spatial scale of <2000 km, along narrow but well-defined latitudinal and depth-dependent gradients. We also asked how microbes are adapted to gradients and extremes in irradiance, temperature, salinity, and nutrients, examining the responses of individual gene ortholog groups to these parameters. Functional and taxonomic metrics were equally well explained (75–79%) by environmental parameters. However, only functional and not taxonomic covariation patterns were conserved when comparing with an intruding water mass with different physicochemical properties. Temperature explained the most variation in each metric, followed by nitrate, chlorophyll, phosphate, and salinity. That nitrate explained more variation than phosphate suggested nitrogen limitation, consistent with low surface N:P ratios. Covariation of gene ortholog groups with environmental parameters revealed patterns of functional adaptation to the challenging Red Sea environment: high irradiance, temperature, salinity, and low nutrients. Nutrient acquisition gene ortholog groups were anticorrelated with concentrations of their respective nutrient species, recapturing trends previously observed across much larger distances and environmental gradients. This dataset of metagenomic covariation along densely sampled environmental gradients includes online data exploration supplements, serving as a community resource for marine microbial ecology.

Introduction

Microbial communities play a central role in energy flow and carbon and nutrient cycling in the oceans. Shotgun sequencing and analysis of microbial community DNA (metagenomics) is now an established method for understanding the microbial genomic diversity underlying these processes (DeLong et al., 2006; Dinsdale et al., 2008). Distribution of microbial diversity and biogeochemistry is structured in large part by environmental gradients in light, temperature, oxygen, salinity, and nutrients. Oceanographic surveys spanning such environmental gradients, combining metagenomic sequencing and measurement of continuous environmental variables, are enabling quantitative understanding of microbial communities (Gianoulis et al., 2009; Raes et al., 2011). Global oceanographic surveys have sequenced hundreds of surface and moderately deep (epipelagic and mesopelagic) ocean microbial communities (Rusch et al., 2007; Sunagawa et al., 2015), cataloging the vast genomic diversity of ocean microbes; further analyses of these data have identified correlations between environmental parameters and genetic community traits (gene ortholog groups and pathways) with predictive power (Gianoulis et al., 2009; Raes et al., 2011; Barberán et al., 2012). Local studies at individual ocean sites, meanwhile, have shown how microbial taxa and gene ortholog groups are partitioned at greater detail along the water column and between discrete ocean environments (DeLong et al., 2006; Coleman and Chisholm, 2010; Ghai et al., 2010; Thompson et al., 2013). Depth is a critical factor behind community structure in the open ocean (DeLong et al., 2006), and dense sampling is capable of capturing subtle changes in environmental parameters with sufficient replication for statistical power.

The Red Sea is an ideal oceanic site for dense sampling of metagenomes to study environment–microbe covariation. The Red Sea is a deep (>2000 m) incipient ocean with strong latitudinal and depth-dependent gradients in temperature, salinity, oxygen, and nutrients (Edwards, 1987). Like the open-ocean gyres of the Atlantic and Pacific Oceans, the Red Sea is oligotrophic with surface waters dominated by the picoplankton *Prochlorococcus* and *Pelagibacter* (Ngugi and Stingl, 2012). More so than these open-ocean gyres, however, the Red Sea lies at pelagic extremes of irradiance, temperature, and salinity. The Red Sea experiences a late-summer southern influx of water called the Gulf of Aden Intermediate Water (GAIW), a foreign water mass that is cooler, fresher, and more nutrient-rich than the native Red Sea water mass. The Red Sea is compact enough to sample across these gradients and water masses on a single month-long expedition, sampling more densely along transects and deeper through the water column than possible on a global survey.

We undertook a high-resolution metagenomic survey of the Red Sea, conducting a multivariate community analysis of covariation between environmental parameters and metagenome-derived taxonomic and functional metrics. We followed three main lines of questioning. First, how well can both taxonomic and functional microbial diversity be explained by environmental parameters, and which environmental parameters explain the most variation? Sunagawa et al. (2015) showed in a recent global ocean survey that temperature could explain more variation in taxonomic abundance than any other parameter. At smaller spatial scales and narrower temperature ranges, does temperature still have the most explanatory power? Which parameters can best explain residual variation? Second, are patterns of environmental covariation conserved across co-occurring water masses? Sampling the GAIW allowed us to determine whether this co-occurring water mass follows the same organizational principles (covariation with environmental parameters) as the native Red Sea water mass, across different taxonomic and functional metrics. Third, how are microbes functionally adapted along environmental gradients of irradiance, temperature, salinity, and nutrients, including extremes in these parameters? Do marine communities exhibit fine-scale genomic adaptation to environmental parameters as has been observed between separate oceans? Our dataset has allowed us to address these questions, and supporting online resources will make the processed data available to the wider community for further investigations.

Materials and methods

Oceanographic sampling

Samples were collected aboard the R/V *Aegaeo* on Leg 1 of the 2011 KAUST Red Sea Expedition, 15 September–11 October 2011. At eight stations, 20 L seawater was collected from each of depths 10, 25, 50, 100, 200, and 500 m; in two cases (Stations 12 and 34) where the seafloor was shallower than 500 m, the deepest sample was taken at the seafloor. Water was collected in 10-L Niskin bottles (i.e., two Niskin bottles per depth), attached to a CTD rosette. Back on deck, the seawater was filtered through a series of three 293-mm mixed cellulose esters filters (Millipore, Billerica, MA) of pore sizes 5.0 μm , 1.2 μm , and 0.1 μm . Filters were placed in sealed plastic bags and frozen at $-20\text{ }^{\circ}\text{C}$. Station properties (location, depth of mixed layer, chlorophyll maximum, and oxygen minimum) are described in Table S1. Physical oceanographic measurements (pressure, temperature, conductivity, chlorophyll *a*, turbidity, and dissolved oxygen) were collected on a modified SeaBird 9/11+ rosette/CTD system, described in Supplementary Methods. Nutrient measurements (nitrate+nitrite, nitrite, ammonium, phosphate,

and silicate) on the final 0.1- μm filtrate were carried out at the UCSB Marine Science Institute and the Woods Hole Oceanographic Institution (Supplementary Methods). Sample water properties are described in Table S2.

DNA extraction and whole-genome shotgun (WGS) sequencing of community metagenomes

Community DNA was extracted from the 0.1- μm filters (0.1-1.2 μm size fraction) using phenol-chloroform extraction, similar to Rusch et al. (2007) and Ngugi et al. (2012); the full protocol is described in Supplementary Methods. Yields of genomic DNA ranged from 200–1500 ng per sample. WGS libraries were made using the Nextera DNA Library Prep Kit (Illumina, San Diego, CA). Median insert size by sample ranged from 183–366 bp (Table S3). Libraries were sequenced using Illumina HiSeq 2000 paired-end (2 x 100 bp) sequencing, filling a total of three lanes (15 samples/lane). Sequence length after adapter removal was 93 bp, and 10 million reads (for each of reads 1 and 2) per sample were generated (Table S3). Reads were quality filtered and trimmed using PRINSEQ (Schmieder and Edwards, 2011) with parameters given in Table S4, and final read counts and metagenome sizes are given in Table S3. Although exact duplicates and reverse-complement exact duplicates were removed, we tested the effect of leaving in these duplicates, and it increased the number of reads retained by only 0.1–0.2%. Raw fastq files have been submitted to the NCBI BioSample database with accession numbers PRJNA289734 (BioProject) and SRR2102994–SRR2103038 (SRA). All analyses presented here were carried out on the quality filtered and trimmed reads. Both reads 1 and 2 were analyzed initially; however, unless otherwise indicated, only the results of read 1 are presented here because of a high degree of redundancy between results of reads 1 and 2. Genomic assemblies were built from each sample; these assemblies were used to calculate insert sizes of metagenomic libraries (Table S3) but provided limited value for quantitation of taxa and gene ortholog groups. The assemblies did, however, yield contigs belonging to uncharacterized clades, which are the subject of a separate study (Haroon et al., in review).

Calculation of metagenomic ‘response variables’ from metagenomic reads

Data tables of merged environmental metadata and response variables are provided in Supplementary Information. Scripts used in the preparation of this manuscript are available at <https://github.com/cuttlefishh/papers> in the directory red-sea-spatial-series.

Taxonomic composition. The 45 metagenomes were analyzed at the read level for the relative abundance of taxonomic groups using CLARK. CLARK (full mode) (Ounit et al., 2015) and CLARK-S (spaced mode) (Ounit and Lonardi, 2015) were used to classify paired metagenomic reads at species and genus level, respectively, based on a k-mer approach against the NCBI RefSeq database (Release 74). CLARK was run using default parameters but with the –highconfidence option, which reports only results with high confidence (assignments with confidence score ≥ 0.75 and gamma value ≥ 0.03), as suggested by the developers. For both species-level and genus-level CLARK results, the column Proportion_All(%) (relative normalized abundance such that each sample sums to 100%) was exported and merged with sample metadata (environmental parameters) using the Python package Pandas. Hierarchically-clustered heatmaps were generated using MetaPhlAn2 utilities (Truong et al., 2015).

In order to specifically capture the diversity within the *Pelagibacter* and *Prochlorococcus* groups in the Red Sea, we used GraftM (<https://github.com/geronimp/graftM>), which classifies reads based on HMM profiles in concert with a reference phylogeny. HMM profiles of *Pelagibacter* 16S rRNA gene and *Prochlorococcus rpoCI* were generated from forward reads

using HMMer v3.1b1 (Eddy, 2011). Reference phylogenies were constructed using MEGA6 (Tamura et al., 2013) from ClustalW alignments (Larkin et al., 2007) of publicly available *Pelagibacter* 16S rRNA gene sequences (Luo et al., 2015) and *Prochlorococcus rpoC1* (DNA-directed RNA polymerase subunit gamma) genes (Shibl et al., in review). Phylogenies were estimated by maximum-likelihood using the GTR+I+G model of nucleotide evolution, chosen with the Perl script ProteinModelSelection.pl that comes with RAxML (Stamatakis 2014). GraftM was run with default parameters based on the the built GraftM packages, which are available here: <https://github.com/fauziharoon/graftm-packages>. Counts were fourth-root transformed.

Gene ortholog group and pathway relative abundance. The 45 metagenomes were analyzed for the relative abundance of gene ortholog groups (KEGG orthologs or KOs) and biochemical pathways (KEGG pathways) using HUMAnN v0.99 (Abubucker et al., 2012) with KEGG release 66.0. First, because the focus of this study was prokaryote genomes, and to increase search speed, reads were recruited to only the prokaryotic fraction of the KEGG genome database, containing all (as of the KEGG release) 1377 prokaryotic genomes (proteomes translated from open reading frames) using a translated search with USEARCH v7.0.1001 (Edgar, 2010) with options `-ublast`, `-accel 0.8`, and `-evalue 1e-5`. The fraction of reads mapped to the KEGG genome database averaged 26.2% (range 16.2–42.5%) across 45 samples (Table S6). Using these results, HUMAnN was run in both standard mode (all taxa merged) and in “per-organism” mode (option: `c_fOrg = True`). KO counts and KEGG pathway counts were normalized to counts per million (CPM) counts, i.e., the number of reads mapped to the KO (or pathway) divided by the sum of all reads mapped in that sample times $1e6$, such that all values for a given sample sum to 1 million. Note that KO counts were not normalized to gene size (e.g., average length of each KO in KEGG) because this was unnecessary: comparisons of KO relative abundances were to environmental parameters and not to each other, and the multivariate community models used are insensitive to absolute magnitudes.

Statistical analyses

We utilized multivariate statistical techniques to relate an array of environmental parameters to metagenomic response variables: taxon relative abundance, KO relative abundance, and pathway relative abundance. All analyses were completed using R v3.1.1 (www.r-project.org) and PERMANOVA+ (Anderson et al., 2008).

Exploratory analyses. Pearson correlations between pairwise combinations of environmental parameters were calculated and displayed as a heat map. Similarity profile analysis (SIMPROF) was used to identify significant groupings within the KO relative abundance response matrix using the *clustsig* package (<http://cran.r-project.org/web/packages/clustsig/index.html>). Partitioning around medoids (PAM) was used to partition the KOs by relative abundance using the *cluster* package v1.15.2 (Kaufman and Rousseeuw, 2005) with Kullback–Leibler distances (Kullback and Leibler, 1951); 12 clusters were chosen based on minimization of the gap statistic.

Explaining variability using environmental parameters. To quantify the spatial variation (both horizontally and vertically) in the response variable matrices explained by the co-occurring gradients in our environmental parameters, we used a multivariate distance-based linear model (DistLM) (McArdle and Anderson, 2001). Eight environmental parameters were considered: temperature, salinity, dissolved oxygen, chlorophyll, turbidity, nitrate, phosphate, and silicate. These parameters were normalized and fitted in a conditional manner to each response variable

matrix using step-wise selection and 9999 permutations of the residuals under a reduced model. Model selection was based on Akaike's information criterion with a second-order bias correction applied (AICc) (Hurvich and Tsai, 1989). The best-fit model (the one that balanced performance with parsimony) was then visualized using distance-based redundancy analysis (dbRDA) (McArdle and Anderson, 2001) in order to identify the directionality of the correlations between the response variable matrix and the environmental parameters. Variation explained by all parameters combined was calculated by forcing all parameters to be included in the final model.

Visualization of metagenome–environment relationships. Pairwise relationships between environmental parameters and KO relative abundance plus other metagenomic response variables were visualized using scatter plots, available using Bokeh-based HTML files in Supplementary Information. Environmental parameters and metagenomic response variables were visualized in the 3D volume of the Red Sea using the `ili` Toolbox, also available in Supplementary Information. KOs having strong correlations with environmental parameters were visualized with canonical correspondence analysis (CCA) using the *vegan* 2.3-1 package, implemented according to Legendre and Legendre (2012). For clarity, only KOs with abundance in the top half and variance in the top tenth of all KOs were visualized by CCA (Supplementary Methods).

Results & Discussion

Overview of Red Sea metagenomic dataset and analysis

To measure covariation of microbial diversity with oceanic gradients, we sampled a north–south transect of the Red Sea at eight stations (Table S1), sampling six depths from the surface to 500 m (Figure 1A), totaling 45 samples. Concurrent with microbial sampling we measured temperature, salinity, dissolved oxygen, chlorophyll *a*, turbidity, nitrate, phosphate, and silicate (values in Table S2, covariance matrix in Figure 2). The microbial size fraction (0.1–1.2 μm) was sequenced at 10M reads per sample with 93-bp paired reads (Table S3). From the metagenomic reads, we calculated five metagenomic response variables: genus-level taxon relative abundance, species-level taxon relative abundance, gene ortholog group (KEGG Orthology or KO) relative abundance, KEGG pathway coverage, and KEGG pathway relative abundance. Of the 1738 taxa, 5775 KOs, and 162 pathways detected in the metagenomes, many exhibited ecologically meaningful correlations with environmental parameters. As an example, the inverse relationship between phosphate concentration and relative abundance of phosphate-acquisition gene *pstS* (K02040) is shown in Figure 1. Samples generally grouped by depth, as indicated by hierarchical clustering of samples based on all taxa (Figure 3) and KOs (Figure S1), and by abundance patterns of individual taxa and KOs (Figures 1B and 5 and Supplementary Information).

The acquired set of metagenomic response variables and environmental parameters allowed us to assess the predictive power of environmental parameters at multiple levels of microbial genotype. We tested how much variation in genus-level taxonomy, KO relative abundance, and pathway relative abundance could be explained using a small number of environmental parameters. Distance-based multivariate linear models (DistLM) and redundancy analysis were used, balancing parsimony and performance (using AICc) to derive an optimal model for explaining variation in each response variable (Figure 4). We acknowledge that the analyses presented here, by necessity, are constrained by the databases available for assigning taxonomy and KOs and the available mappings of KOs to pathways.

Variation in metagenomic diversity metrics explained by environmental parameters

We first asked which environmental parameters explained the most variation in both taxonomic and functional diversity metrics, and we looked for differences in total variation explained. Environmental parameters explained similar amounts of variation in the various metrics used (Figure 4A). Total variation explained using all available environmental parameters was only marginally higher for KO relative abundance (79.0%) than for pathway relative abundance (77.0%) and genus-level taxon relative abundance (75.1%). Variation explained was similar even at greater phylogenetic resolution within two important marine microbial groups, the autotroph *Prochlorococcus* and the heterotroph *Pelagibacter* (SAR11 clade), which are the two most abundant genera across our dataset (Figure 3). At ecotype-level taxonomy (*Prochlorococcus* “ecotypes” and *Pelagibacter* “subclades”) and genus-level KO abundance, the percent variation explained was similar to the community as a whole (Figure 4B).

Overall, environmental parameters explained more variation in our dataset than in other microbial ecosystems where this has been tested. For example, in a similarly sized dataset on reef-associated microbes, the best parameter explained only 15% of taxonomic variation and 18% of metabolic variation (Kelly et al., 2014). Variations in water column microbial communities appear easier to predict. In an English Channel time-series, day length explained over 65% of variance in taxonomic diversity (Gilbert et al., 2011). The better performance of water column data could be because the open ocean is not patchy but well mixed and stably stratified by depth into layers, especially in the Red Sea in late summer. Relative to open-water samples, the increased complexity of the response matrix in reef-associated samples resulting from microhabitats and higher diversity likely reduces model performance.

Temperature explained the most variation in each of the response variables; this was followed in each case by nitrate (second) and then chlorophyll (third) for the functional response variables and salinity (third) for genus-level taxonomy (Figures 4A and S2). Although nitrate and phosphate ($r=0.97$) and silicate ($r=0.95$ with nitrate and phosphate) were very highly correlated (Figure 2), nitrate was consistently ranked higher (explaining more variation) than phosphate in the optimal model, and silicate was not implicated (Figure 4A). Across the whole dataset, temperature explained more variation than oxygen in every response variable. Although temperature and oxygen were correlated ($r=0.79$), oxygen was never part of the optimal model. Temperature has been identified as a key predictor of microbial diversity in the ocean by other studies (Johnson et al., 2006; Sunagawa et al., 2015). Specifically, Sunagawa et al. (2015) showed that temperature is a better predictor of taxonomic composition than is oxygen. Here we show that the same is true for gene functional composition (KOs): the absence of oxygen in any optimal model suggests that temperature is a stronger predictor (and possibly also driver) of microbial diversity than oxygen.

Nitrate (measured as nitrate+nitrite) and phosphate both formed part of the optimal model for each functional response variable, with nitrate always explaining slightly more variation than phosphate. This finding hints at the relative selective pressures these two key nutrients exert. The idea that limitation of a given nutrient leads to the gain of genes for uptake and assimilation of that nutrient is supported by numerous studies (Coleman and Chisholm, 2010; Kelly et al., 2013; Thompson et al., 2013). Here we extend that idea to the quantitative explanatory power of the nutrient’s concentration for predicting KO relative abundance. The predictive power of nitrate relative to phosphate in our genetic results may indicate that nitrogen (N) is relatively more limiting than phosphorus (P) in the Red Sea. Limited data exist on this topic, but N:P ratios of 0.3–5 (well below the Redfield ratio of 16, the atomic ratio of N to P in phytoplankton (Redfield,

1958)) in the Gulf of Aqaba (Lindell et al., 2005) and a high frequency of N-acquisition genes in a Red Sea surface metagenome relative to the Atlantic ocean (Thompson et al., 2013) suggest N limitation; however, in the northern Gulf of Aqaba, a P-stress response and lack of N-stress *ntcA* response in Red Sea cyanobacteria supports the opposite conclusion (Post, 2005). Nevertheless, our own nutrient measurements from this cruise show that the N:P ratio (calculated here as the ratio of nitrate+nitrite to phosphate) in surface waters was 2, whereas a prototypical ratio of 16 was observed in deeper waters (Figure S3), possibly due to remineralization of N from phytoplankton at depth. Regarding nitrate, it is interesting that for *Pelagibacter* KO relative abundance, nitrate (59.1%) not temperature explained the most variation. N limitation has strong effects on the transcriptional response of *Pelagibacter* in culture, with genes for assimilation of organic sources of N up-regulated under N stress (Smith et al., 2013). However, none of the differentially expressed genes identified by Smith et al. (2013) covaried strongly with nitrate in our dataset (reads from corresponding KOs assigned to *Pelagibacter*). Thus, the nature of a potential selective force of this putative N limitation on *Pelagibacter* gene content remains a mystery.

Chlorophyll has a non-monotonic relationship with depth, unlike the other environmental parameters analyzed here, which are either low at the surface and high at depth (salinity, phosphate, nitrate, silicate) or high at the surface and low at depth (temperature, oxygen, turbidity). Chlorophyll peaks below the surface mixed layer at the deep chlorophyll maximum (100 m in the Red Sea, Table S1), due to a confluence of sunlight from above, nutrients from below, and the tendency of deeper phytoplankton to possess higher chlorophyll per cell. Because chlorophyll is effectively orthogonal to other environmental parameters, it should not be unexpected that it has significant explanatory power, and that chlorophyll and temperature (a key depth-dependent parameter) together could explain much of the genetic variation.

Comparison with a foreign water mass

We next asked whether the ability to predict metagenomic response variation from environmental parameters was sufficiently robust to extend to alternate water masses. Fortunately, the Red Sea experiences a water influx each summer from the Indian Ocean, called the Gulf of Aden Intermediate Water (GAIW), which was captured in three of our samples. The GAIW brings cooler, less saline, oxygen-rich, nutrient-rich water from the Gulf of Aden (Churchill et al., 2014). The three GAIW samples were clearly distinct from their neighboring samples in the temperature–salinity (T–S) profile (Figure S4A) and Red Sea water column (Figure S4B). The properties of GAIW samples resembled those of deeper samples in the native Red Sea water mass; the GAIW samples, which were from 50–100 m depth, had markedly different environmental parameters from non-GAIW samples from 50–100 m. We were curious if our multivariate community models would be able to highlight any differences between response variables in model performance across different water masses.

Considering the distance-based redundancy analysis (Figures 4A and S2), all of the functional metrics placed the GAIW samples amidst the native Red Sea samples, though clustering with deeper samples, owing to the lower temperature and higher nutrients of the GAIW samples. The taxonomic metrics, however, placed the GAIW samples either far apart from the other samples (genus-level) or with much deeper samples than expected even based on physicochemical properties (species-level), driven by the high nitrate and low temperature and salinity of the GAIW samples relative to the non-GAIW samples (Figure 4A). These results suggest that environmental covariation patterns of taxonomy are less conserved across water

masses (i.e., different combinations of environmental parameters) than are environmental covariation patterns of functional metrics.

Supporting the idea that functional covariation with environmental parameters is conserved across different water masses, we note anecdotally that for most of the individual environment–KO relationships examined below (Figure 5), GAIW samples followed a similar pattern to the non-GAIW majority. One notable exception was salinity, with the salinity of GAIW much lower than anything in the native Red Sea water mass and the covariation of KOs with salinity very different for GAIW samples compared to non-GAIW samples.

Environmental covariation patterns of individual KOs

We finally turned our attention to the covariation patterns of individual KOs, which partition along the three-dimensional water column in ecologically meaningful ways. Which KOs have the strongest covariation with environmental parameters? Can previously observed patterns between oceans also be observed along gradients within a single sea? Which KOs are implicated in the adaptive response of microbes to the low nutrients and high irradiance, temperature, and salinity of the Red Sea?

We used canonical correspondence analysis (CCA) to identify and visualize correlations between KOs and environmental parameters, with KOs organized by metabolic pathway (Figure 6 and Table S9). We note that all KOs were included in the distance-based linear model above, whereas a subset of the most differentially represented and abundant KOs are shown in the CCA (methods); most of the KOs discussed below are visualized in Figure 6. Additionally, KOs were ranked by total abundance across all samples (Table S7), and KO abundance patterns were clustered using partitioning around medoids (PAM) into 12 clusters (Table S8).

Nutrient acquisition and energy metabolism contributed most of the functional covariation with environmental parameters (Figure 6). The patterns documented here were not exclusively depth-dependent but also captured subtle covariation with gradients along isobaths. The full set of environmental parameters and metagenomic response variables can be visualized interactively in the 3D volume of the Red Sea using web-based tools with files in Supplementary Information. Visualization examples showing the temperature–salinity profile, and temperature in the 3D volume of the Red Sea, are provided in Figure S4.

Depth is a spatial parameter that is not ‘felt’ by microorganisms, except as it relates to pressure, but nevertheless structures virtually all environmental parameters in the water column. Light attenuates with depth, and thus photosynthesis is mostly confined to the upper 200 m of the water column. As expected, KOs for photosynthesis were most abundant in shallow waters and gradually less abundant in deeper waters. This was true for both oxygenic (*psbA*/K02703) and anoxygenic (*pufL*/K08928) photosynthesis, photosynthetic electron transport (*petH*/K02641, *ndhD*/K05575), and pigment biosynthesis (*por*/K00218) (Figure 5). Some heterotrophic bacteria accumulate carbon-rich polymers called polyhydroxyalkanoates when organic carbon is readily available but growth is limited by nutrients (Stubbe et al., 2005). We observed that polyhydroxyalkanoate synthase (*phbC*/K03821) was more abundant in mesopelagic samples than epipelagic samples, consistent with relatively more heterotrophy than phototrophy at depth.

Temperature covaries with depth (warmer at surface, colder at depth), but in the Red Sea southern surface waters are warmer than northern surface waters, and the GAIW is cooler than surrounding depths in the native Red Sea water mass. We observed that KOs for chaperonins, including heat-shock proteins GroEL/ES (K04077, K04078), and proteases, including Clp

protease (*clpP*/K01358), had greater relative abundance in warm (24–32°C) samples than in cooler (21–23°C) samples (Figure 5). Both GroEL/ES (Zeilstra-Ryalls et al., 1991) and Clp protease (Zybailov et al., 2009) have important roles in protein folding, which is sensitive to high temperature. The increase in *groEL* relative abundance leveled off above 23 °C, whereas the increase in *clpP* relative abundance increased along the full temperature range from 21 to 32 °C. In an opposite trend, glycolysis was relatively more abundant in colder samples than warmer samples, as exemplified by phosphofructokinase (*pfk*/K00850). This is likely related to the relative increase in heterotrophy at depth, as deeper waters tend to be cooler. The most cold, eutrophic samples from the GAIW have the highest relative abundance of *pfk* by far, indicating relatively more heterotrophy in this foreign water mass.

Salinity in the Red Sea is higher at depth and in northern surface waters and lower in southern surface waters and the GAIW. Saline-rich waters of the the Mediterranean and Red Seas were previously shown to have high relative abundance of genes for degradation of osmolytes, in particular recruiting to *Pelagibacter* (Thompson et al., 2013). We put forth a hypothesis that high salinity leads to high production of osmolytes by algae and other organisms, a valuable organic carbon and nutrient source for *Pelagibacter* (Sun et al., 2011), and therefore there is selective pressure to encode osmolyte-degrading enzymes (Thompson et al., 2013). Across the 45 Red Sea metagenomes, KOs for glycine betaine (GBT) transport and degradation (Sun et al., 2011) – glycine betaine/proline transporter (*proV*/K02000), betaine-homocysteine S-methyltransferase (*bhmT*/K00544), dimethylglycine dehydrogenase (DMGDH/K00315), and sarcosine oxidase (*soxB*/K00303) – were correlated with high chlorophyll and with high or moderate salinity (Figure 6). The shape of covariation of these four KOs was not as clearly dependent on salinity as we expected (Figure 5). As suggested by the CCA plot (Figure 6), both salinity and chlorophyll help explain the relative abundance of GBT transport and degradation KOs. The legend at top-right of Figure 5 indicates chlorophyll *a* fluorescence of the samples as a function of depth. Among the GBT-utilization KOs, samples with either high chlorophyll (green and yellow-black) or high salinity (blue and purple) tended to have the highest abundance. Thus this multifaceted trend is completely consistent with the hypothesis of phototroph (chlorophyll) production of osmolytes in high-salinity waters as a source of reduced carbon and nutrients for heterotrophic bacteria. Regarding the phototrophs responsible for producing GBT, we note that while *Prochlorococcus* are thought to use glucosylglycerate and sucrose as their main osmolytes, some low-light *Prochlorococcus* strains and *Synechococcus* strains are thought to accumulate GBT as well (Scanlan et al., 2009), and these low-light strains are more abundant in the high-chlorophyll samples. Interestingly, the KO patterns with reads assigned to *Pelagibacter* specifically (e.g., *proV*/K02000) – one- to two-thirds of the recruited reads for these salinity-related KOs – were similar to the overall KO patterns but more dependent on salinity than chlorophyll (Figure 5).

Phosphate and nitrate are both low in Red Sea surface waters but higher at depth and in the GAIW (for example, phosphate shown in Figure 1A). Several studies have shown that genes for nutrient acquisition are enriched in waters limited for those nutrients, e.g., phosphate acquisition in the low-phosphate Mediterranean and Sargasso Seas (Coleman and Chisholm, 2010; Kelly et al., 2013; Thompson et al., 2013). Across the gradients of the Red Sea, numerous KOs for nutrient transport and assimilation were differentially distributed between nutrient-poor (surface and non-GAIW) and nutrient-rich (deep and GAIW) samples. Although depth was a major factor underlying the covariation observed here, we also detected more subtle differences along gradients within isobaths, as well as more striking differences between GAIW and non-GAIW samples at the same depth. This is to our knowledge the first demonstration of differential

abundance patterns of nutrient-acquisition genes on such a small scale, not between disparate oceans but across environmental gradients within a single sea.

Phosphate-acquisition and phosphate-response KOs were enriched in low-phosphate samples (Figure 5), including phosphate ABC transporter (*pstS*/K02040), phosphate two-component system PhoBR (K07657, K07636), alkaline phosphatase (*phoA*/K01077), and phosphate stress-response protein PhoH (K06217). Trends were observed even within isothermal samples binned in two-degree increments, both for cooler isotherms with a wide range of phosphate concentrations, and for warmer isotherms with a narrow and low range of phosphate concentrations, e.g. *phoB*/K07657 (Figure S5). Phosphonate-acquisition genes, in an opposite pattern, were enriched in high-phosphate (and low-chlorophyll) samples, as exemplified by the phosphonate ABC transporter (*phnD*/K02044). Phosphonate utilization genes (*phn*) are abundant in proteobacteria such as *Pelagibacter* (Villarreal-Chiu et al., 2012), and are enriched in deeper waters of the Sargasso Sea (Martinez et al., 2010) and generally in low-P waters (Coleman and Chisholm, 2010; Feingersch et al., 2010). Although phosphonate-acquisition genes are found in some *Prochlorococcus* in the environment (Feingersch et al., 2012), genomes and transcriptional responses of cultured strains (Martiny et al., 2006) suggest that inorganic phosphate is the major P source for *Prochlorococcus*. Therefore, in addition to ecotype-level genome variability tuned to ambient concentrations of phosphate and phosphonate (Martiny et al., 2006), different distributions of phosphate- and phosphonate-acquisition genes along the water column are likely also due to genus-level differences in taxonomic composition (and therefore gene content) along the water column, for example, phosphate-utilizing *Prochlorococcus* in the epipelagic and phosphonate-utilizing *Pelagibacter* in the mesopelagic. Indeed, many of the low-nutrient-associated KOs such as phosphate and urea transporters had very similar abundance patterns to KOs typical of a phototrophic bacterium like *Prochlorococcus*: photosystems and photosynthetic electron transport, chlorophyll binding proteins, the Calvin cycle, and transport and chelation of metal cofactors essential for photosynthesis (PAM cluster 8, Table S8).

Nitrogen-acquisition KOs were differentially distributed with respect to nitrate concentration and, like with phosphorus, also followed one of two opposite patterns (Figure 5), which were also observed within isotherms (Figure S5). KOs for urea transport (*urtA*/K11959) and assimilatory ferredoxin–nitrate reductase (*narB*/K00367) were enriched in low-nitrate relative to high-nitrate samples. Conversely, KOs for ammonium transport (*amt*/K03320), nitrite reductase (*nirK*/K00368), and nitrate reductase-like protein (*narX*/K00369) were enriched in high-nitrate relative to low-nitrate samples, with the shift to high abundance occurring at 5 μM for *amt* and 15 μM for *nirK* and *narX*. Opposite of *narB*, *narX* was most abundant in the mesopelagic, where oxygen was low (1 mL/L at 500 m); this is consistent with a putative nitrate reductase fusion gene (*narX*) being up-regulated under anaerobic conditions in *Mycobacterium* (Hutter and Dick, 1999). Our measurements of N species besides nitrate were either below detection (nitrite) or unreliable (ammonium), but using global averages, nitrite and ammonium peak around the chlorophyll maximum and nitracline (where nitrate increases most rapidly) and then decrease through the deep epipelagic and mesopelagic (Gruber, 2008); urea is generally low and patchy through the water column (Remsen, 1971). Abundance patterns of several N-acquisition KOs thus appear to follow the “low nutrient–high KO” paradigm: nitrate reductase was abundant where nitrate was low (surface), and ammonium transport and nitrite reductase were abundant where ammonium and nitrite were low (mesopelagic). Urea transport, if it follows the same paradigm, indicates that urea in the surface of the Red Sea is also very low relative to depth.

Conclusions

We have analyzed a 3D array of marine metagenomes across environmental gradients in the Red Sea, showing that three-quarters of taxonomic and functional variation could be explained by temperature, nitrate, and chlorophyll. Covariation patterns with environmental parameters were largely conserved across water masses, notably more so for gene orthologs and pathways than for taxonomic groups. Individual patterns of KO covariation with environmental parameters revealed protein folding functions highly correlated with temperature, osmolyte degradation functions correlated with salinity and chlorophyll, and acquisition functions of nitrogen and phosphorus species anti-correlated with concentrations of their respective species. Subtle trends shown here across isobathic and isothermal gradients have hitherto been observed only between distant and disparate oceans. It is expected that this high-resolution marine metagenomic map of the Red Sea, accessible using interactive visualization tools, will serve as an important resource for marine microbiology and modeling.

Conflict of interest

The authors declare no conflict of interest.

References

- Abubucker SS, Segata NN, Goll JJ, Schubert AAM, Izard JJ, Cantarel BBL et al. (2012). Metabolic reconstruction for metagenomic data and its application to the human microbiome. *PLoS Comput Biol* **8**: e1002358–e1002358.
- Anderson MJ. (2001). A new method for non-parametric multivariate analysis of variance. *Austral Ecol* **26**: 32–46.
- Anderson MJ, Gorley RN, Clarke KR. (2008). *PERMANOVA+ for PRIMER: guide to software and statistical methods*. PRIMER-E.
- Anderson MJ, Robinson J. (2003). Generalized discriminant analysis based on distances. *Aust NZ J Stat* **45**: 301–318.
- Anderson MJ, Willis TJ. (2003). Canonical Analysis of Principal coordinates: a useful method of constrained ordination for ecology. *Ecology* **84**: 511–525.
- Barberán A, Fernández-Guerra A, Bohannan MJB, Casamayor EO. (2012). Exploration of community traits as ecological markers in microbial metagenomes. *Mol Ecol* **21**: 1909–1917.
- Churchill JH, Bower AS, McCorkle DC, Abualnaja Y. (2014). The transport of nutrient-rich Indian Ocean water through the Red Sea and into coastal reef systems. *J Mar Res* **72**: 165–181.
- Coleman ML, Chisholm SW. (2010). Ecosystem-specific selection pressures revealed through comparative population genomics. *Proc Natl Acad Sci USA* **107**: 18634–18639.
- DeLong EF, Preston CM, Mincer T, Rich V, Hallam SJ, Frigaard N et al. (2006). Community genomics among stratified microbial assemblages in the ocean's interior. *Science* **311**: 496–503.
- Dinsdale EA, Edwards RA, Hall D, Angly F, Breitbart M, Brulc JM et al. (2008). Functional metagenomic profiling of nine biomes. *Nature* **452**: 629–632.
- Eddy SR. (2011). Accelerated profile HMM searches. *PLoS Comput Biol* **7**: e1002195.
- Edgar RC. (2010). Search and clustering orders of magnitude faster than BLAST. *Bioinformatics (Oxford, England)* **26**: 2460–2461.
- Edwards FJ. (1987). Climate and oceanography. In: *Key Environments: Red Sea*, AJ Edwards SM Head, ed., pages 45–68. Pergamon.
- Feingersch R, Suzuki MT, Shmoish M, Sharon I, Sabeji G, Partensky F et al. (2010). Microbial community genomics in eastern Mediterranean Sea surface waters. *ISME J* **4**: 78–87.
- Feingersch RR, Philosof AA, Mejuch TT, Glaser FF, Alalouf OO, Shoham YY et al. (2012). Potential for phosphite and phosphonate utilization by *Prochlorococcus*. *ISME J* **6**: 827–834.
- Ghai R, Martin-Cuadrado A.-B, Molto AG, Heredia IG, Cabrera R, Martin J et al. (2010). Metagenome of the Mediterranean deep chlorophyll maximum studied by direct and fosmid library 454 pyrosequencing. *ISME J* **4**: 1154–1166.
- Gianoulis TA, Raes J, Patel PV, Bjornson R, Korbel JO, Letunic I et al. (2009). Quantifying environmental adaptation of metabolic pathways in metagenomics. *Proc Natl Acad Sci USA* **106**: 1374–1379.

- Gilbert JA, Steele JA, Caporaso JG, Steinbrück L, Reeder J, Temperton B et al. (2011). Defining seasonal marine microbial community dynamics. *ISME J* **6**: 298–308.
- Gruber N. (2008). The marine nitrogen cycle: overview and challenges. In: *Nitrogen in the Marine Environment*, DG Capone, DA Bronk, MR Mulholland, EJ Carpenter, ed. Elsevier.
- Haroon MF, Thompson LR, Parks DH, Hugenholtz P, Stingl U. A catalogue of 136 microbial draft genomes from the Red Sea. In review, *Scientific Data*.
- Hurvich CM, Tsai C.-L. (1989). Regression and time series model selection in small samples. *Biometrika* **76**: 297–307.
- Hutter B, Dick T. (1999). Up-regulation of narX, encoding a putative α -fused nitrate reductaseTM in anaerobic dormant Mycobacterium bovisBCG. *FEMS Microbiol Lett* **178**: 63–69.
- Johnson ZI, Zinser ER, Coe A, McNulty NP, Woodward SEM, Chisholm SW. (2006). Niche partitioning among Prochlorococcus ecotypes along ocean-scale environmental gradients. *Science* **311**: 1737–1740.
- Kaufman L, Rousseeuw PJ. (2005). *Finding Groups in Data: An Introduction to Cluster Analysis*. Wiley Series in Probability and Statistics. Wiley-Interscience.
- Kelly L, Ding H, Huang KH, Osburne MS, Chisholm SW. (2013). Genetic diversity in cultured and wild marine cyanomyovirus reveals phosphorus stress as a strong selective agent. *ISME J* **7**: 1827–1841.
- Kelly LW, Williams GJ, Barott KL, Carlson CA, Dinsdale EA, Edwards RA et al. (2014). Local genomic adaptation of coral reef-associated microbiomes to gradients of natural variability and anthropogenic stressors. *Proc Natl Acad Sci U S A* **111**: 10227–10232.
- Kettler GC, Martiny AC, Huang K, Zucker J, Coleman ML, Rodrigue S et al. (2007). Patterns and implications of gene gain and loss in the evolution of Prochlorococcus. *PLoS Genet* **3**: e231.
- Kullback S, Leibler RA. (1951). On information and sufficiency. *Ann Math Statist* **22**: 79–86.
- Larkin MA et al. (2007). Clustal W and Clustal X version 2.0. *Bioinformatics (Oxford, England)* **23**, 2947–2948.
- Legendre P, Legendre L. (2012). *Numerical Ecology*. Elsevier.
- Lindell D, Penno S, Al-Qutob M, David E, Rivlin T, Lazar B et al. (2005). Expression of the nitrogen stress response gene ntcA reveals nitrogen-sufficient Synechococcus populations in the oligotrophic northern Red Sea. *Limnology and Oceanography* **50**: 1932–1944.
- Lindgreen S, Adair KL, Gardner PP. (2016). An evaluation of the accuracy and speed of metagenome analysis tools. *Sci Rep* **6**: 19233.
- Luo H, Thompson LR, Stingl U, Hughes AL. (2015). Selection Maintains Low Genomic GC Content in Marine SAR11 Lineages. *Mol Biol Evol* **32**: 2738–2748.
- Martinez A, Tyson GW, DeLong EF. (2010). Widespread known and novel phosphonate utilization pathways in marine bacteria revealed by functional screening and metagenomic analyses. *Environ Microbiol* **12**: 222–238.
- Martiny AC, Coleman ML, Chisholm SW. (2006). Phosphate acquisition genes in Prochlorococcus ecotypes: Evidence for genome-wide adaptation. *Proc Natl Acad Sci USA* **103**: 12552–12557.
- Matsen FA, Kodner RB, Armbrust EV. (2010). pplacer: linear time maximum-likelihood and Bayesian phylogenetic placement of sequences onto a fixed reference tree. *BMC Bioinformatics* **11**: 538–538.
- McArdle BH, Anderson MJ. (2001). Fitting multivariate models to community data: a comment on distance-based redundancy analysis. *Ecology* **82**: 290–297.
- Ngugi DK, Antunes A, Brune A, Stingl U. (2012). Biogeography of pelagic bacterioplankton across an antagonistic temperature-salinity gradient in the Red Sea. *Mol Ecol* **21**: 388–405.
- Ngugi DK, Stingl U. (2012). Combined analyses of the ITS loci and the corresponding 16S rRNA genes reveal high micro- and macrodiversity of SAR11 populations in the Red Sea. *PLoS ONE* **7**: e50274.
- Ounit R, Lonardi S. (2015). Higher Classification Accuracy of Short Metagenomic Reads by Discriminative Spaced k-mers. In: *Algorithms in Bioinformatics. 15th International Workshop, WABI 2015*, pages 286–295. Springer Berlin Heidelberg.
- Ounit R, Wanamaker S, Close TJ, Lonardi S. (2015). CLARK: fast and accurate classification of metagenomic and genomic sequences using discriminative k-mers. *BMC Genomics* **16**: 236.
- Perna NT, Plunkett G, Burland V, Mau B, Glasner JD, Rose DJ et al. (2001). Genome sequence of enterohaemorrhagic Escherichia coli O157:H7. *Nature* **409**: 529–533.
- Post AF. (2005). Nutrient limitation of marine cyanobacteria. In: *Harmful Cyanobacteria*, J Huisman, HC. P Matthijs, PM Visser, ed., pages 87–107. Springer.
- Quast C, Pruesse E, Yilmaz P, Gerken J, Schweer T, Yarza P et al. (2012). The SILVA ribosomal RNA gene database project: improved data processing and web-based tools. *Nucleic Acids Res* **41**: D590–D596.
- Raes J, Letunic I, Yamada T, Jensen LJ, Bork P. (2011). Toward molecular trait-based ecology through integration of biogeochemical, geographical and metagenomic data. *Mol Syst Biol* **7**: 473–473.

- Redfield AC. (1958). The biological control of chemical factors in the environment. *American Scientist*: 205–221.
- Remsen CC. (1971). The Distribution of Urea in Coastal and Oceanic Waters. *Limnology and Oceanography* **16**: 732–740.
- Rusch DB, Halpern AL, Sutton G, Heidelberg KB, Williamson S, Yooseph S et al. (2007). The Sorcerer II Global Ocean Sampling expedition: northwest Atlantic through eastern tropical Pacific. *PLoS Biol* **5**: e77.
- Scanlan DJ, Ostrowski M, Mazard S, Dufresne A, Garczarek L, Hess WR et al. (2009). Ecological genomics of marine picocyanobacteria. *Microbiol Mol Biol Rev* **73**: 249–299.
- Schmieder R, Edwards R. (2011). Quality control and preprocessing of metagenomic datasets. *Bioinformatics (Oxford, England)* **27**: 863–864.
- Smith DP, Thrash JC, Nicora CD, Lipton MS, Burnum-Johnson KE, Carini P et al. (2013). Proteomic and transcriptomic analyses of "Candidatus Pelagibacter ubique" describe the first PII-independent response to nitrogen limitation in a free-living Alphaproteobacterium. *mBio* **4**: e00133–12.
- Stamatakis A. (2014). RAxML version 8: a tool for phylogenetic analysis and post-analysis of large phylogenies. *Bioinformatics (Oxford, England)* doi:10.1093/bioinformatics/btu033
- Stubbe J, Tian J, He A, Sinskey AJ, Lawrence AG, Liu P. (2005). Nontemplate-dependent polymerization processes: polyhydroxyalkanoate synthases as a paradigm. *Annu Rev Biochem* **74**: 433–480.
- Sunagawa S, Coelho LP, Chaffron S, Kultima JR, Labadie K, Salazar G et al. (2015). Ocean plankton. Structure and function of the global ocean microbiome. *Science* **348**: 1261359–1261359.
- Sun J, Steindler L, Thrash JC, Halsey KH, Smith DP, Carter AE et al. (2011). One carbon metabolism in SAR11 pelagic marine bacteria. *PLoS ONE* **6**: e23973.
- Tamura K, Stecher G, Peterson D, Filipowski A, and Kumar S. (2013). MEGA6: Molecular Evolutionary Genetics Analysis Version 6.0. *Mol Biol Evol* **30**: 2725–2729.
- Thompson LR, Field C, Romanuk T, Ngugi D, Siam R, El Dorry H et al. (2013). Patterns of ecological specialization among microbial populations in the Red Sea and diverse oligotrophic marine environments. *Ecol Evol* **3**: 1780–1797.
- Truong DT, Franzosa EA, Tickle TL, Scholz M, Weingart G, Pasolli E et al. (2015). MetaPhlan2 for enhanced metagenomic taxonomic profiling. *Nat Methods* **12**: 902–903.
- Villarreal-Chiu JF, Quinn JP, McGrath JW. (2012). The genes and enzymes of phosphonate metabolism by bacteria, and their distribution in the marine environment. *Front Microbiol* **3**: 1–13.
- Wood DE, Salzberg SL. (2014). Kraken: ultrafast metagenomic sequence classification using exact alignments. *Genome Biol* **15**: R46.
- Zaneveld JR, Lozupone C, Gordon JI, Knight R. (2010). Ribosomal RNA diversity predicts genome diversity in gut bacteria and their relatives. *Nucleic Acids Res* **38**: 3869–3879.
- Zeilstra-Ryalls J, Fayet O, Georgopoulos C. (1991). The Universally Conserved GroE (Hsp60) Chaperonins. *Annu Rev Microbiol* **45**: 301–325.
- Zybailov B, Friso G, Kim J, Rudella A, Rodriguez VR, Asakura Y et al. (2009). Large Scale Comparative Proteomics of a Chloroplast Clp Protease Mutant Reveals Folding Stress, Altered Protein Homeostasis, and Feedback Regulation of Metabolism. *Mol Cell Proteomics* **8**: 1789–1810.

Acknowledgments

We thank chief scientist Amy Bower, co-chief scientist Yasser Abualnaja, Leah Trafford, Dan McCorkle, and other scientists from the Woods Hole Oceanographic Institution, the captain and crew of the R/V *Aegaeo* and the Hellenic Center for Marine Research, and Red Sea Research Center Director James Luyten for their help on the 2011 KAUST (King Abdullah University of Science and Technology) Red Sea Expedition. Assistance with DNA extraction was provided by Matt Cahill, David Ngugi, and Francisco Acosta Espinosa. Bioinformatics assistance was provided by Mamoon Rashid and James Morton. Statistics assistance was provided by Mikyoung Jun, Myoungji Lee, Yoan Eynaud, and James Morton. We thank Jon Sanders, Jenan Kharbush, and Lihini Aluwihare for helpful comments on the manuscript. We also thank colleagues who suggested KOs hypothesized to have interesting ecological patterns: Paul Berube, Yue Guan, Laura Villanueva, Francisco Rodríguez-Valera, Nathan Ahlgren, Zhenfeng Liu, Francy Jiménez,

and Ulrike Pfreundt. This work was funded in part by a postdoctoral fellowship to L.R.T. from the Saudi Basic Industries Corporation (SABIC).

Author Contributions L.R.T. planned the study, organized the cruise, collected samples, curated physical and chemical data, extracted DNA, processed sequence data, generated graphics and tables, and wrote the paper. G.J.W. planned and executed statistical analyses and wrote the paper. M.F.H. tested and ran taxonomic analyses and wrote the paper. A.S. collected samples and extracted DNA. P.L. ran metabolite prediction analysis. J.S. generated interactive visualizations. R.K. provided analytical input and wrote the paper. U.S. planned the study, organized the cruise and wrote the paper.

Author Information Sequence data have been submitted to the NCBI BioSample database with accession numbers PRJNA289734 (BioProject) and SRR2102994–SRR2103038 (SRA).

Figures

Figure 1: Covariation of gene ortholog group abundance and environmental parameters in the water column. (A) 3D contour map of the Red Sea, with outlines (isobaths) showing boundaries of the Red Sea at sampling depths, and samples colored by phosphate concentration (outer circle) and relative abundance of gene ortholog group (KO) for phosphate ABC transporter *pstS* (inner circle). (B) Scatter plot of KO relative abundance versus phosphate concentration. Samples taken within the foreign water mass Gulf of Aden Intermediate Water (GAIW) are indicated. KO relative abundance is given in units of counts per million (CPM) of total KO counts in each sample (i.e., all KOs sum to 1 million in each sample).

Figure 2: Pearson correlations between environmental parameters shown as a colored covariance matrix. A Pearson's r value of 1 (red) indicates a total positive correlation, a value of -1 (blue) indicates a total negative correlation, and a value of 0 (white) indicates no correlation.

Figure 3: Relative abundance of genera across metagenomes displayed as a hierarchically-clustered heatmap, with clustering of samples by Bray-Curtis distance (top dendrogram) and clustering of taxa by correlation between samples (left dendrogram), with branch colors indicating major clusters. GAIW sample labels are colored red. The top 50 most abundant genera are shown. Relative abundances of all 683 genera detected for each sample sum to 100. Genus-level taxonomy was calculated based on k-mer frequency in comparison with the NCBI RefSeq database (methods).

Figure 4: Maximization of linear relations between environmental parameters and metagenomic response variables using a distance-based multivariate linear model and distance-based redundancy analysis for (A) the whole data set and (B) genera *Prochlorococcus* and *Pelagibacter* (see methods). Percent variation explained by each parameter is shown as a bar graph. The optimal model using AICc to balance performance and parsimony is shown for both (A) and (B); also shown for (A) is the remainder of variation explained by other environmental parameters unused in the optimal model. The dbRDA ordination of the optimal model is shown along dbRDA axes 1 and 2, with stations colored by depth and water mass (GAIW in black).

Figure 5: Covariation of select KOs with environmental parameters. KO relative abundance is given in units of counts per million of total KO counts in each sample (i.e., all KOs sum to 1 million in each sample).

Figure 6: Canonical correspondence analysis of KO relative abundance with environmental parameters. Samples are shown as black numerals indicating depth in meters (GAIW samples marked with asterisk), environmental parameters as dark blue arrows, and KOs colored by KEGG pathway. For clarity, only KOs were displayed that were found in all samples, with a total count of at least one per thousand counts over all samples, and variance in the top 10% (see methods). The large arrow indicates the trend of sample position from surface (epipelagic), to deep chlorophyll maximum, to deep (mesopelagic).

Supplementary Information

Supplementary Methods

Physical and chemical measurements of seawater

Oceanographic measurements were collected on a modified SeaBird 9/11+ rosette/CTD system. Sensors on the CTD included those for pressure, temperature and conductivity (SBE9+ CTD), chlorophyll *a* and turbidity (WETLabs), and dissolved oxygen (SeaBird). Seawater samples were collected at nearly all stations for shipboard calibrations of salinity and oxygen CTD measurements. For nutrient measurements, filtrate from the final 0.1- μm filters was collected and frozen at $-20\text{ }^{\circ}\text{C}$, then analyzed by flow injection analysis at the UCSB Marine Science Institute (nitrate+nitrite, nitrite, ammonium, and phosphate) and the Woods Hole Oceanographic Institution (silicate). Ammonium was measured at less than $2\text{ }\mu\text{M}$ and nitrite at less than $0.7\text{ }\mu\text{M}$ for all samples; these data were determined to be insufficiently precise for statistical analyses because nitrite concentrations were near or below the detection limit and the ammonium measurements could not be done on fresh (unfrozen) samples.

DNA extraction

Filters were cut aseptically into small pieces and placed in tubes. Lysis buffer (0.1 M Tris-HCl, 0.1 M Na-EDTA, 0.1 M $\text{Na}_2\text{H}_2\text{PO}_4$, 1.5 M NaCl, pH 8.0) was added to a volume of 15 mL. Three cycles of freeze-thaw ($-80\text{ }^{\circ}\text{C}$, then $65\text{ }^{\circ}\text{C}$) were carried out. Lysozyme (2.5 mg/mL final conc.) and RNase A (2 mg/mL final conc.) was added, and the tubes were heated with rotation at $37\text{ }^{\circ}\text{C}$ for 1 h. Next, proteinase K (0.2 mg/mL final conc.) and SDS (1% final conc.) was added, and the tubes were heated with rotation at $55\text{ }^{\circ}\text{C}$ for 2 h. Lysate was extracted with an equal volume of phenol:chloroform:isoamyl alcohol (25:24:1), then an equal volume of chloroform:isoamyl alcohol (24:1). DNA was concentrated and washed with 10 mM TE (pH 8.0) using Amicon Ultra filters (10 kDa MWCO). Finally, DNA was ethanol precipitated for additional purity.

Additional statistical exploratory analyses

Testing for zonation patterns across depth gradients was carried out using a hypothesis-driven, constrained approach to test whether clear gradients existed in microbial diversity across depth (fixed factor), a prediction supported by numerous studies to date (DeLong et al., 2006; Ngugi and Stingl, 2012). We used a permutational multivariate analysis of variance (PERMANOVA) (Anderson, 2001), with subsequent pairwise comparisons, to formally test for differences in multivariate response variables across six a priori defined depth zones (10, 25, 50, 100, 200, 500 m). Analyses were based on Bray–Curtis similarity matrices, type III (partial) sums-of-squares, and unrestricted permutations of the raw data. The results of the PERMANOVA were visualized using a canonical analysis of principal coordinates (CAP) (Anderson and Willis, 2003), with allocation success (Anderson and Robinson, 2003) quantified across groups. Allocation success (expressed as a percentage) gave a measure of how distinct one depth group was relative to all other depth groups in the CAP multivariate space. Multidimensional scaling (MDS) was used to determine similarity between samples using the *vegan* package v2.3-1 (<http://vegan.r-forge.r-project.org/>).

Alternate taxonomy composition methods

In addition to CLARK (main methods), two other metagenomic taxonomy composition methods, described below, were tested. Based on the percent of reads mapping (Table S6), the percent taxonomic variation explained using environmental parameters, and an independent comparison of the methods (Lindgreen et al., 2016), we chose CLARK for determining taxonomic composition of each metagenomic library.

GraftM v0.6.3 (<https://github.com/geronimp/graftM>) employs a Hidden Markov Model (HMM) with pattern recognition to identify 16S rRNA gene sequences (https://www.ora.gov/gsp2015/abstracts/TysonG_02.pdf) and assign them to taxonomic groups based on tree placement using the SILVA database (Release 119, Quast et al. (2012)), to the most granular phylogenetic level possible using pplacer (Matsen et al., 2010). This non-BLAST approach allows more accurate classification regardless of incomplete databases (https://www.ora.gov/gsp2015/abstracts/TysonG_02.pdf). GraftM was then used with default parameters, using forward reads only. Total counts were presence/absence transformed or fourth root transformed.

Kraken (Wood and Salzberg, 2014) attempts to assign taxonomy to each read or read pair using k-mer analysis. Metagenomes were analyzed in ‘paired’ mode using the NCBI RefSeq database. Genus-level counts were normalized to the total number of paired reads per metagenome. Several key genera—‘*Candidatus Pelagibacter ubique*’, hereafter *Pelagibacter*, and groups of phages infecting *Prochlorococcus*, *Synechococcus*, and *Pelagibacter*—were manually curated to include taxa inadequately classified in NCBI Taxonomy. Total counts were normalized to total paired reads.

Kraken and GraftM were not selected because they mapped fewer sequence reads (avg. 8.8% for Kraken genus-level, 0.05% for GraftM genus-level, Table S6) and had lower percent variation explained. Further, a recent comparison of metagenomic taxonomy assignment tools found that CLARK performed best among tools tested in correlation between predicted and known relative abundances with a test data set (Lindgreen et al., 2016).

Total variation explained of species-level taxon relative abundance (Table S5) was similar (76.1%) to genus-level relative abundance (75.1%). Given this similarity, along with the two-fold greater number of reads mapped for genus-level (avg. 11.6%) than species-level (avg. 6.2%) assignment (Table S6) by the k-mer based CLARK software (Ounit et al., 2015) and the observed greater accuracy of genus-level taxonomic assignments, we chose to focus on genus-level taxonomy for analyses.

CCA visualization of metagenome–environment relationships

The filtering described here was used only for selecting KOs to visualize by CCA in the main text (Figure 6); the full set of KOs was used for all other analyses, as well as the CCA of all KOs in Supplementary Information (Figure S6). Starting with all KOs (5775), KOs were sequentially filtered if they were not found in all samples (3311 remained), if they had a relative count abundance across all samples less than one per thousand counts or 0.001 (2455 remained), or if they had variance less than $5e-8$ (252 remained); after CCA, only KOs with non-hypothetical functions were plotted (224 remained). KOs were colored by pathway; note that most KOs belong to multiple KEGG pathways, each with two tiers below ‘Metabolism’. In order to keep the number of pathways displayed to a digestible number, pathways were colored as follows: KOs among the top-ten most represented second-tier pathways were assigned if those pathways had at least five representatives (this corresponded to seven second-tier pathways in Figure 3);

the remaining KOs among the top-ten most represented first-tier pathways were assigned if those pathways had at least five representatives (this corresponded to seven first-tier pathways in Figure 3); the remaining KOs were assign to pathway ‘Other’.

Supplementary Figures

Figure S1: Similarity profile analysis (SIMPROF) of KO relative abundance data using Bray–Curtis similarity. Samples are colored by depth layer, and Gulf of Aden Intermediate Water (GAIW) samples are marked with an asterisk (*).

Figure S2: Distance-based redundancy analysis (dbRDA) plots for each response variable. The dbRDA ordination maximizes linear relations of response variables with the predictors. Environmental parameters in the optimal model to the AICc model are plotted. Percent total variation explained by axes 1 and 2 is given.

Figure S3: N:P ratio, calculated as nitrate+nitrite to phosphate ratio, across samples plotted as **(A)** nitrate+nitrite vs. phosphate and **(B)** depth vs. N:P ratio. Typical Redfield ratio of N:P = 16 is shown as well as the observed N:P = 2 in surface samples.

Figure S4: Temperature–salinity (T–S) relationship shown using publicly available interactive visualization tools. **(A)** T–S profile generated with Bokeh Python package and **(B)** 3D map of Red Sea colored by temperature generated with `ili Toolbox. Points shown are the 45 samples used in this study. The three GAIW foreign water mass samples are clearly visible as distinct from native Red Sea water mass samples by T–S profile and temperature anomaly in the water column.

Figure S5: Covariation of nutrient acquisition KOs with phosphate and nitrate, separated by isotherms in 2-degree increments. KO relative abundance is given in units of counts per million of total KO counts in each sample (i.e., all KOs sum to 1 million in each sample).

Figure S6: Canonical correspondence analysis of KO relative abundance with environmental parameters, with all KOs displayed. Samples are shown as black numerals indicating depth in meters (GAIW samples marked with asterisk), environmental parameters as dark blue arrows, and KOs colored by pathway.

Supplementary Tables

Table S1: Station properties. For each station, the following oceanographic features were calculated from CTD measurements: mixed layer depth (temperature decrease of 0.5 °C from surface), chlorophyll maximum, and oxygen minimum. Values of the chlorophyll maximum and oxygen minimum are given.

Table S2: Sample water properties.

Table S3: Illumina metagenome properties. Number of reads and total size in bp of forward (Fwd) and reverse (Rev) sequenced reads are after PRINSEQ preprocessing.

Table S4: Parameters used in PRINSEQ preprocessing, listed in the order that processing steps were applied.

Table S5: Results of AICc, the stepwise explanation of variation in response variables by sequentially adding environmental parameters (predictors), balancing performance and parsimony.

Table S6: Percent of all forward reads mapped by HUMAnN and taxonomy assignment methods. Columns from left to right: HUMAnN translated search to prokaryotic KO sequences in KEGG; CLARK genus-level k-mer; CLARK species-level k-mer; Kraken genus-level k-mer; GraftM genus-level 16S; GraftM ecotype-level *Prochlorococcus rpoCI*; GraftM ecotype-level *Pelagibacter* 16S.

Table S7: KOs ranked by total abundance across all samples.

Table S8: KOs clustered by total abundance across all samples using partitioning around medoids (PAM) with 12 clusters.

Table S9: Cartesian and polar coordinates of the 224 KEGG KOs (gene ortholog groups) plotted in the CCA ordination. KOs were first assigned to second-tier KEGG pathways (if total pathway count was at least 5), then first-tier KEGG pathways (if total pathway count was at least 5), and the remaining KOs were grouped as 'Other'. Direction is in degrees from the polar axis. For reference, environmental parameter directions are as follows: salinity, 0.5°; chlorophyll, 94.3°; turbidity, 169.6°; oxygen, 171.7°; temperature, -160.5°; depth, -16.9°; nitrate, -11.2°; silicate, -9.4°; phosphate, -9.1°.

Online Content

Interactive 3D maps. Point the Chrome browser to <http://ili-toolbox.github.io/> or install the `ili Toolbox Chrome app. Drag the PNG file then one of the CSV data files to the web page. Use the on-screen menu to change the heatmap appearance; we recommend setting spot border to 1, hotspot quantile to 1, and color map to Blue-Red. Select data categories to view or search for terms in the selection menu. Drag another CSV file to change datasets.

Map file (PNG):

Thompson_RedSea_Map.png

Data files (CSV):

Thompson_RedSea_TaxaRelAbund_Genus.csv
Thompson_RedSea_TaxaRelAbund_Species.csv
Thompson_RedSea_TaxaCounts_Pelagibacter.csv
Thompson_RedSea_TaxaCounts_Prochlorococcus.csv
Thompson_RedSea_KORelativeAbundance_AllTaxa.csv
Thompson_RedSea_KORelativeAbundance_Nitrosopumilus.csv
Thompson_RedSea_KORelativeAbundance_Pelagibacter.csv
Thompson_RedSea_KORelativeAbundance_Prochlorococcus.csv
Thompson_RedSea_PathwayCoverage_AllTaxa.csv
Thompson_RedSea_PathwayRelativeAbundance_AllTaxa.csv

Interactive scatter plots. Open the HTML files in any web browser and choose any set of two environmental parameters or response variables to plot. Type the first few letters to go directly to a selection. Plots can be resized and then saved to PNG.

Plot files (HTML):

Thompson_RedSea_TaxaRelAbund_Genus.html
Thompson_RedSea_TaxaRelAbund_Species.html
Thompson_RedSea_TaxaCounts_Pelagibacter.html
Thompson_RedSea_TaxaCounts_Prochlorococcus.html
Thompson_RedSea_KORelativeAbundance_AllTaxa.html
Thompson_RedSea_KORelativeAbundance_Nitrosopumilus.html
Thompson_RedSea_KORelativeAbundance_Pelagibacter.html
Thompson_RedSea_KORelativeAbundance_Prochlorococcus.html
Thompson_RedSea_PathwayCoverage_AllTaxa.html
Thompson_RedSea_PathwayRelativeAbundance_AllTaxa.html

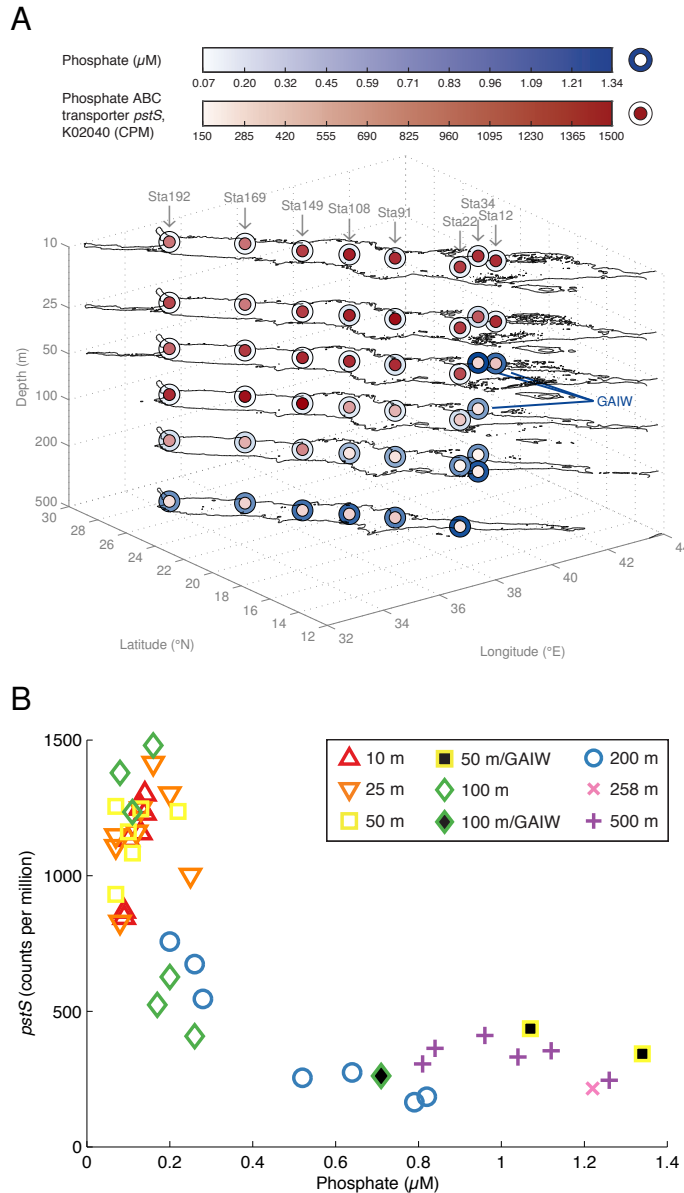


Figure 1. Covariation of gene ortholog group abundance and environmental parameters in the water column. (A) 3D contour map of the Red Sea, with outlines (isobaths) showing boundaries of the Red Sea at sampling depths, and samples colored by phosphate concentration (outer circle) and relative abundance of gene ortholog group (KO) for phosphate ABC transporter *pstS* (inner circle). (B) Scatter plot of KO relative abundance versus phosphate concentration. Samples taken within the foreign water mass Gulf of Aden Intermediate Water (GAIW) are indicated. KO relative abundance is given in units of counts per million (CPM) of total KO counts in each sample (i.e., all KOs sum to 1 million in each sample).

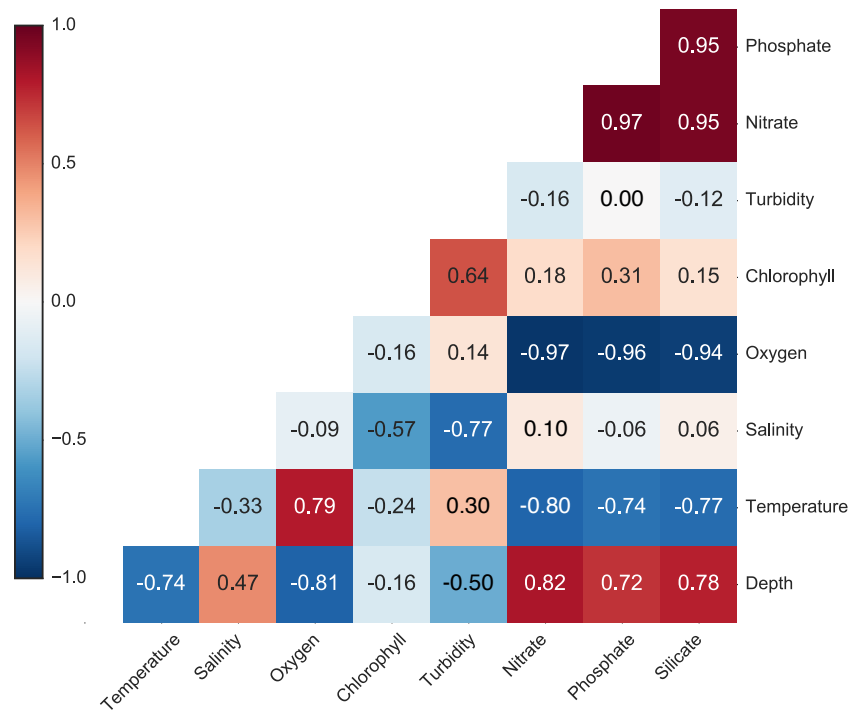


Figure 2. Pearson correlations between environmental parameters shown as a colored covariance matrix. A Pearson's r value of 1 (red) indicates a total positive correlation, a value of -1 (blue) indicates a total negative correlation, and a value of 0 (white) indicates no correlation.

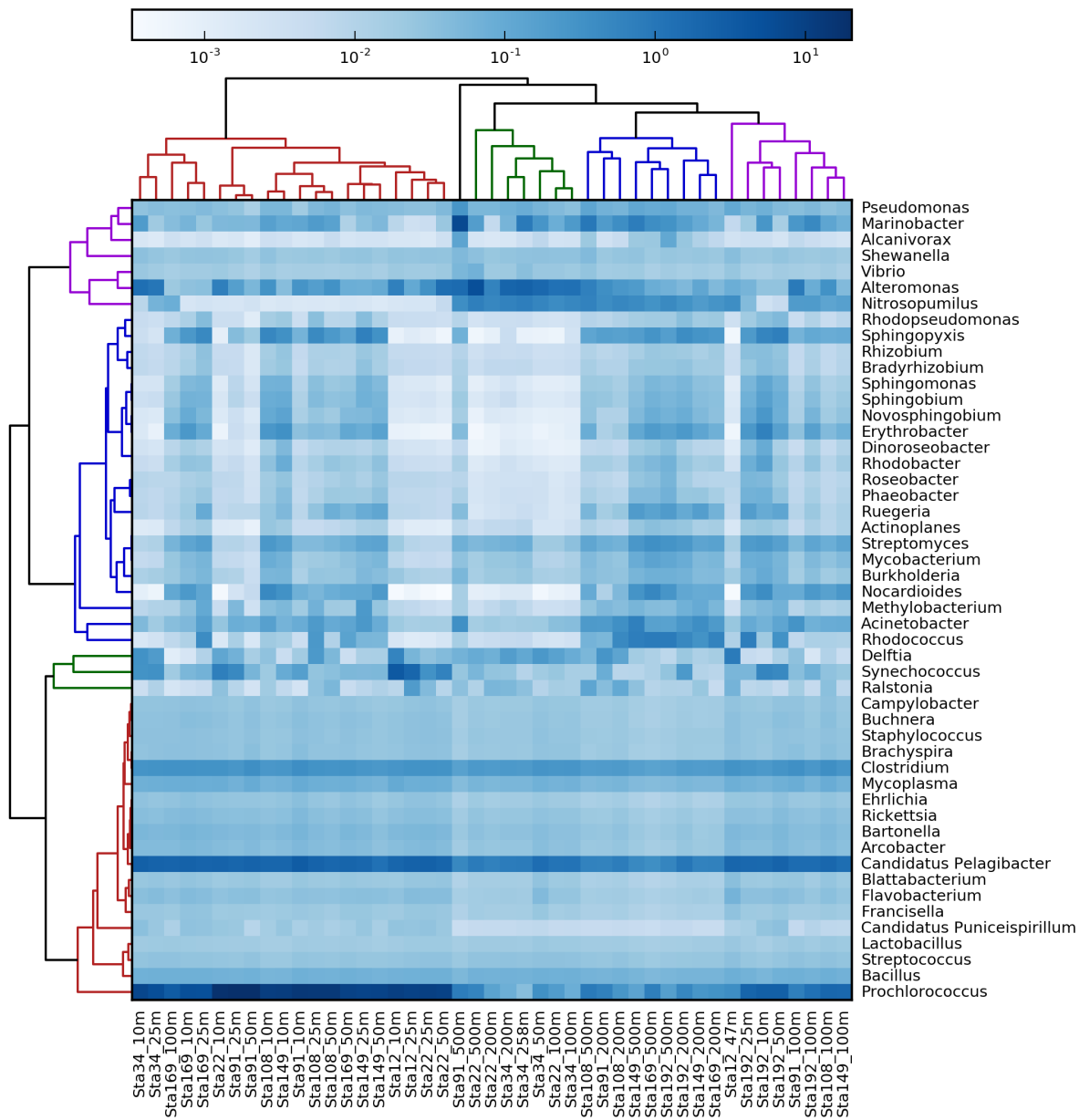


Figure 3. Relative abundance of genera across metagenomes displayed as a hierarchically-clustered heatmap, with clustering of samples by Bray–Curtis distance (top dendrogram) and clustering of taxa by correlation between samples (left dendrogram), with branch colors indicating major clusters. GAIW sample labels are colored red. The top 50 most abundant genera are shown. Relative abundances of all 683 genera detected for each sample sum to 100. Genus-level taxonomy was calculated based on k-mer frequency in comparison with the NCBI RefSeq database (methods).

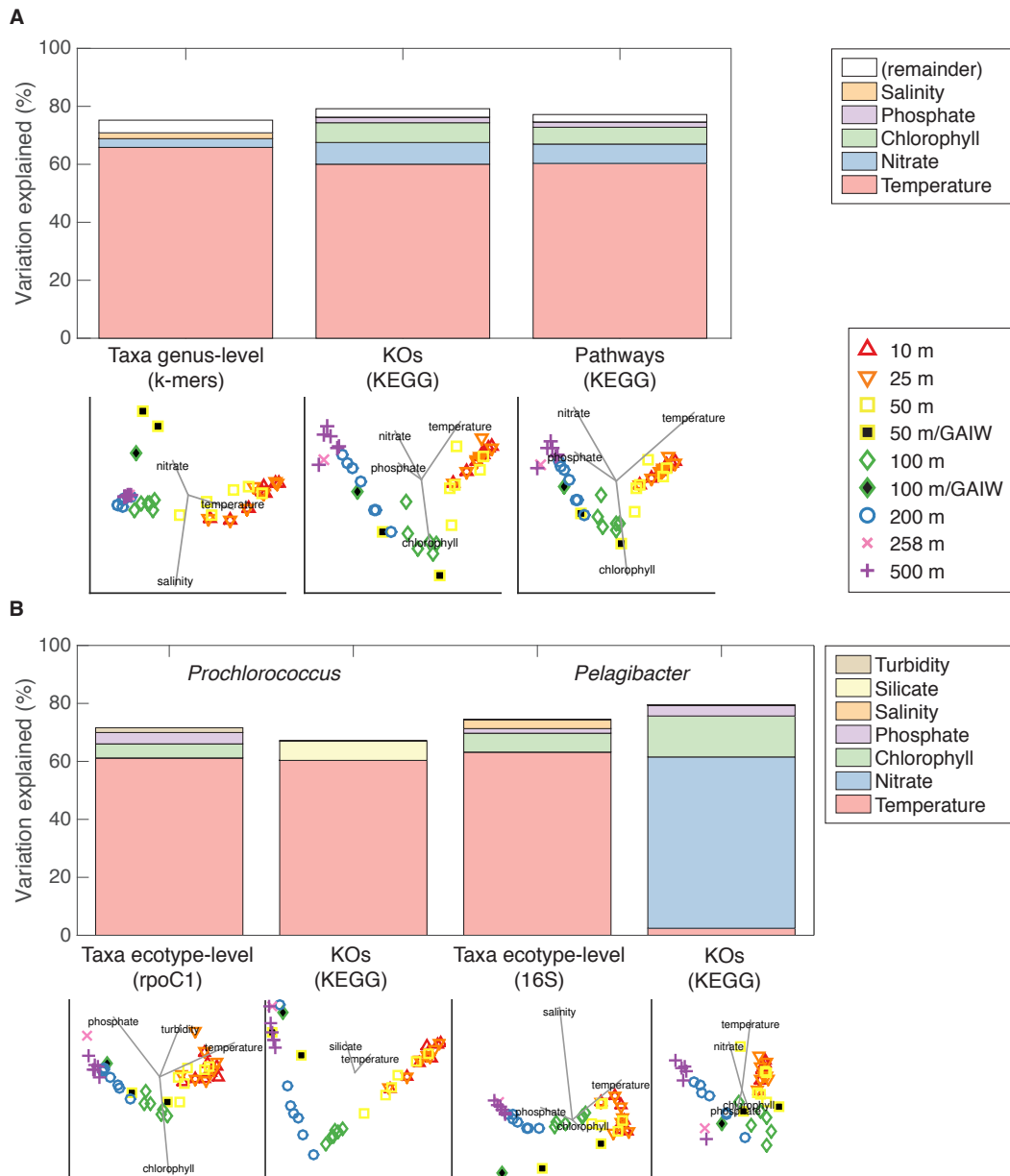


Figure 4. Maximization of linear relations between environmental parameters and metagenomic response variables using a distance-based multivariate linear model and distance-based redundancy analysis for (A) the whole data set and (B) genera *Prochlorococcus* and *Pelagibacter* (see methods). Percent variation explained by each parameter is shown as a bar graph. The optimal model using AICc to balance performance and parsimony is shown for both (A) and (B); also shown for (A) is the remainder of variation explained by other environmental parameters unused in the optimal model. The dbrDA ordination of the optimal model is shown along dbrDA axes 1 and 2, with stations colored by depth and water mass (GAIW in black).

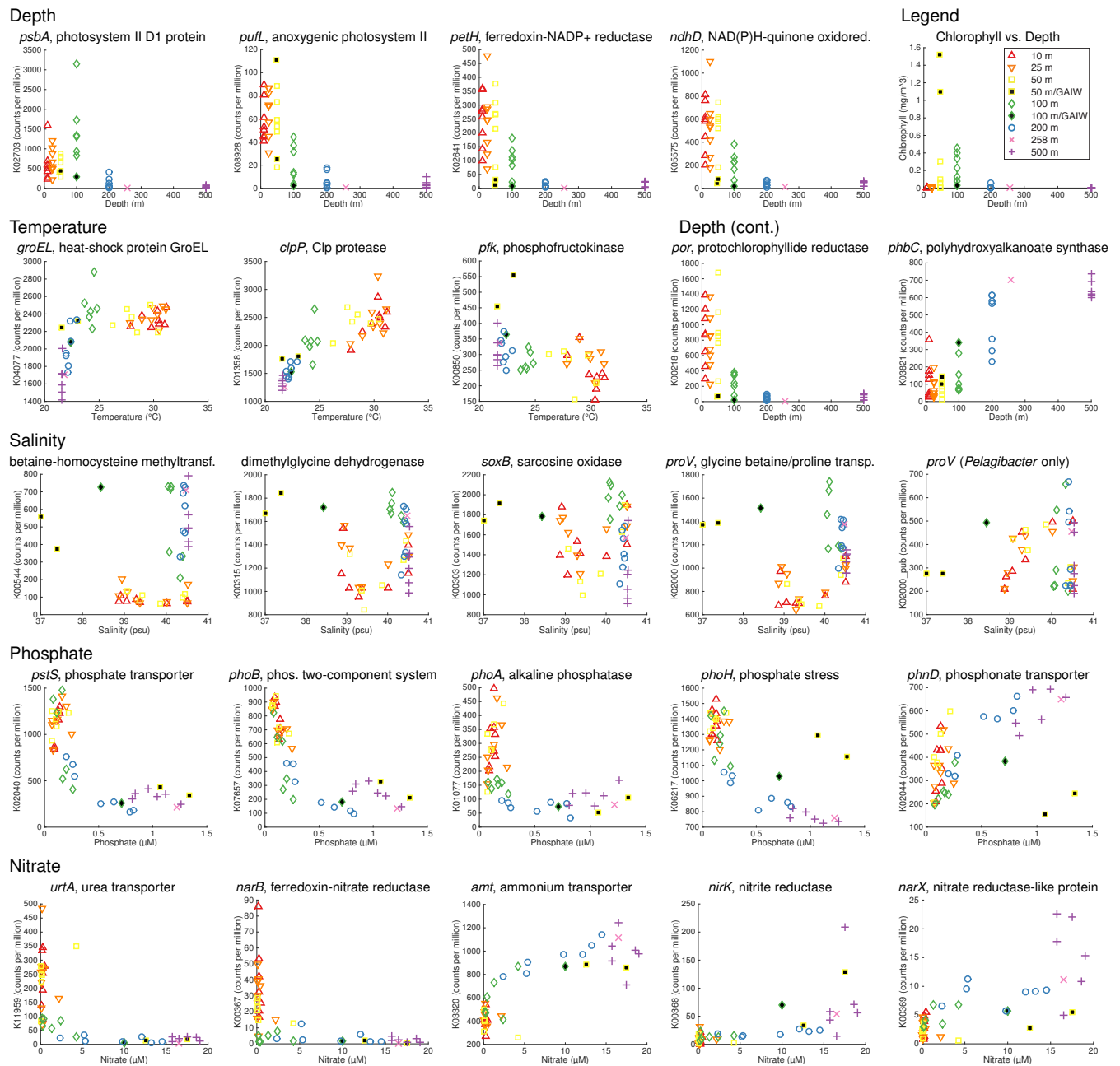


Figure 5. Covariation of select KOs with environmental parameters. KO relative abundance is given in units of counts per million of this total KO counts in each sample (i.e., all KOs sum to 1 million in each sample).

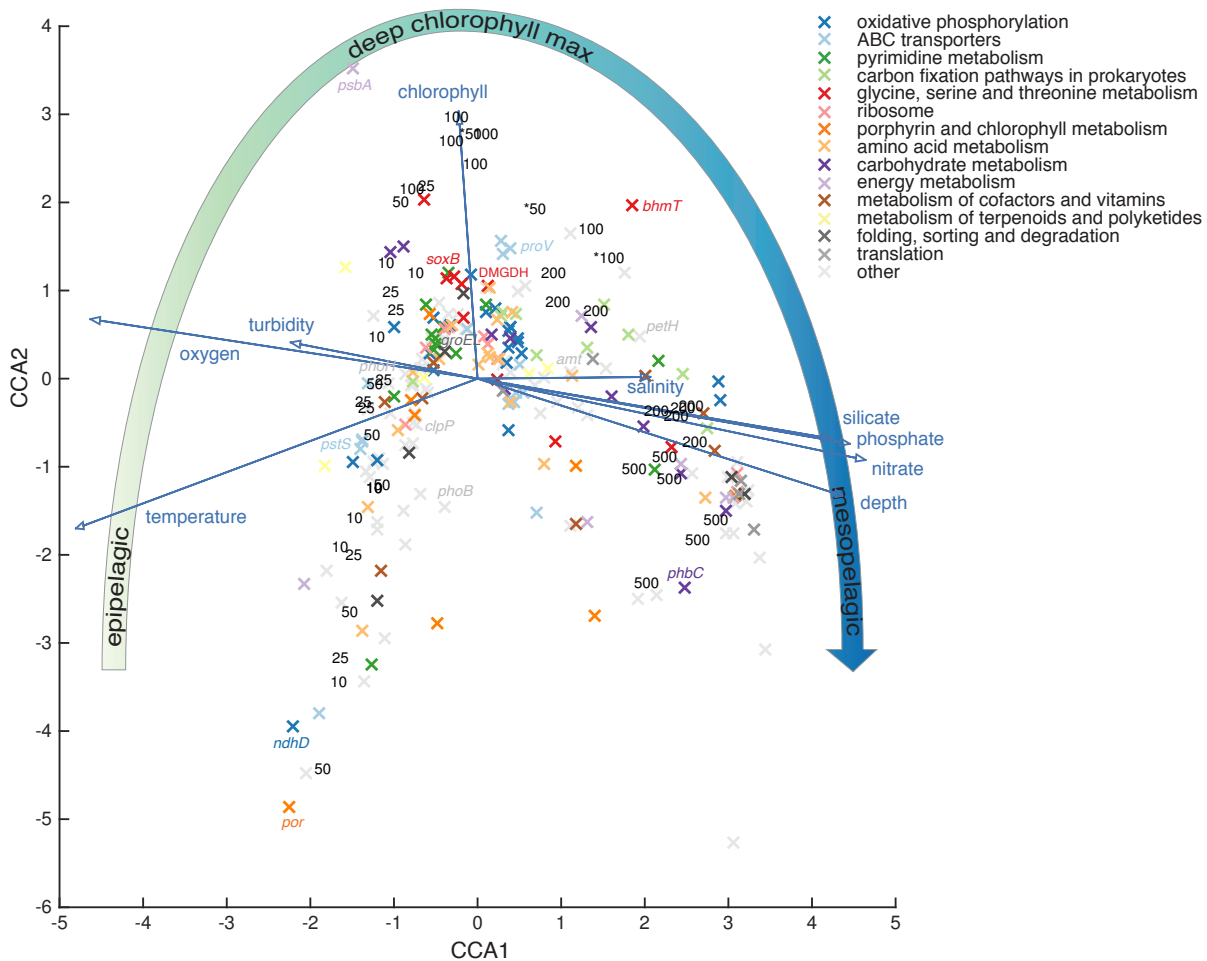


Figure 6. Canonical correspondence analysis of KO relative abundance with environmental parameters. Samples are shown as black numerals indicating depth in meters (GAIW samples marked with asterisk), environmental parameters as dark blue arrows, and KOs colored by KEGG pathway. For clarity, only KOs were displayed that were found in all samples, with a total count of at least one per thousand counts over all samples, and variance in the top 10% (see methods). The large arrow indicates the trend of sample position from surface (epipelagic), to deep chlorophyll maximum, to deep (mesopelagic).

Supplementary Information

Supplementary Figures

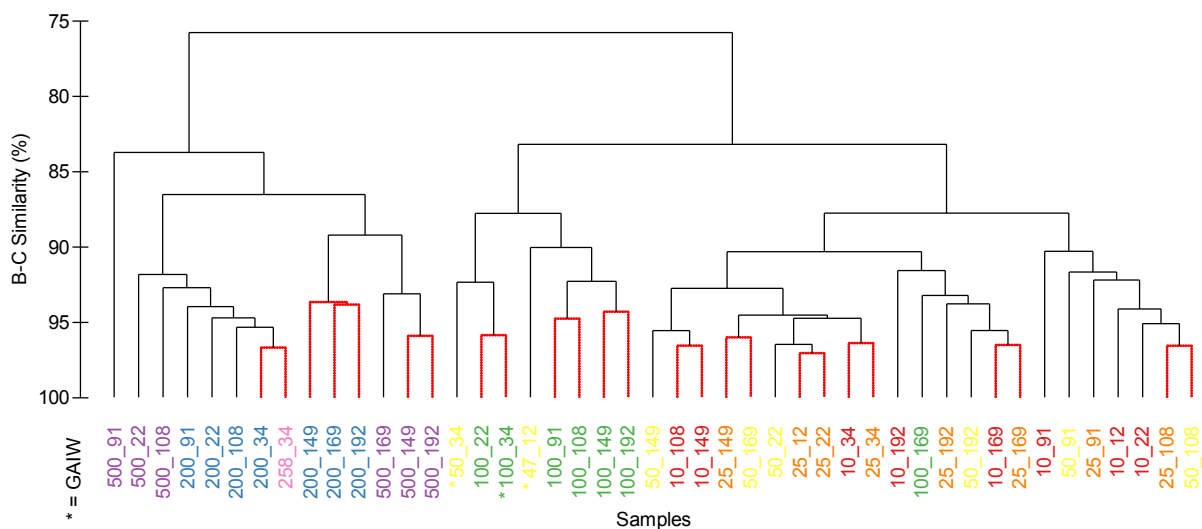


Figure S1. Similarity profile analysis (SIMPROF) of KO relative abundance data using Bray–Curtis similarity. Samples are colored by depth layer, and Gulf of Aden Intermediate Water (GAIW) samples are marked with an asterisk (*).

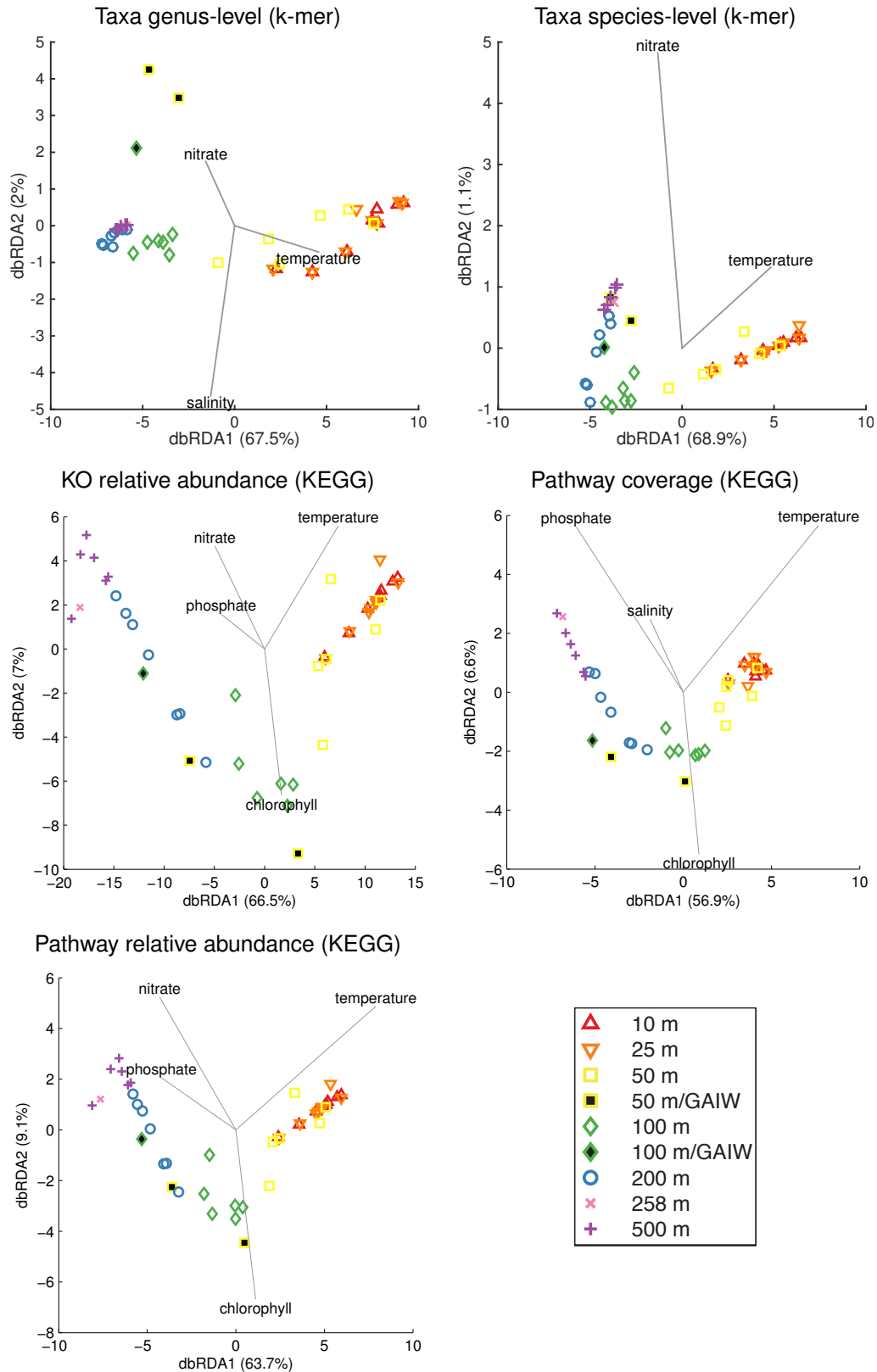


Figure S2. Distance-based redundancy analysis (dbRDA) plots for each response variable. The dbRDA ordination maximizes linear relations of response variables with the predictors. Environmental parameters in the optimal model to the AICc model are plotted. Percent total variation explained by axes 1 and 2 is given.

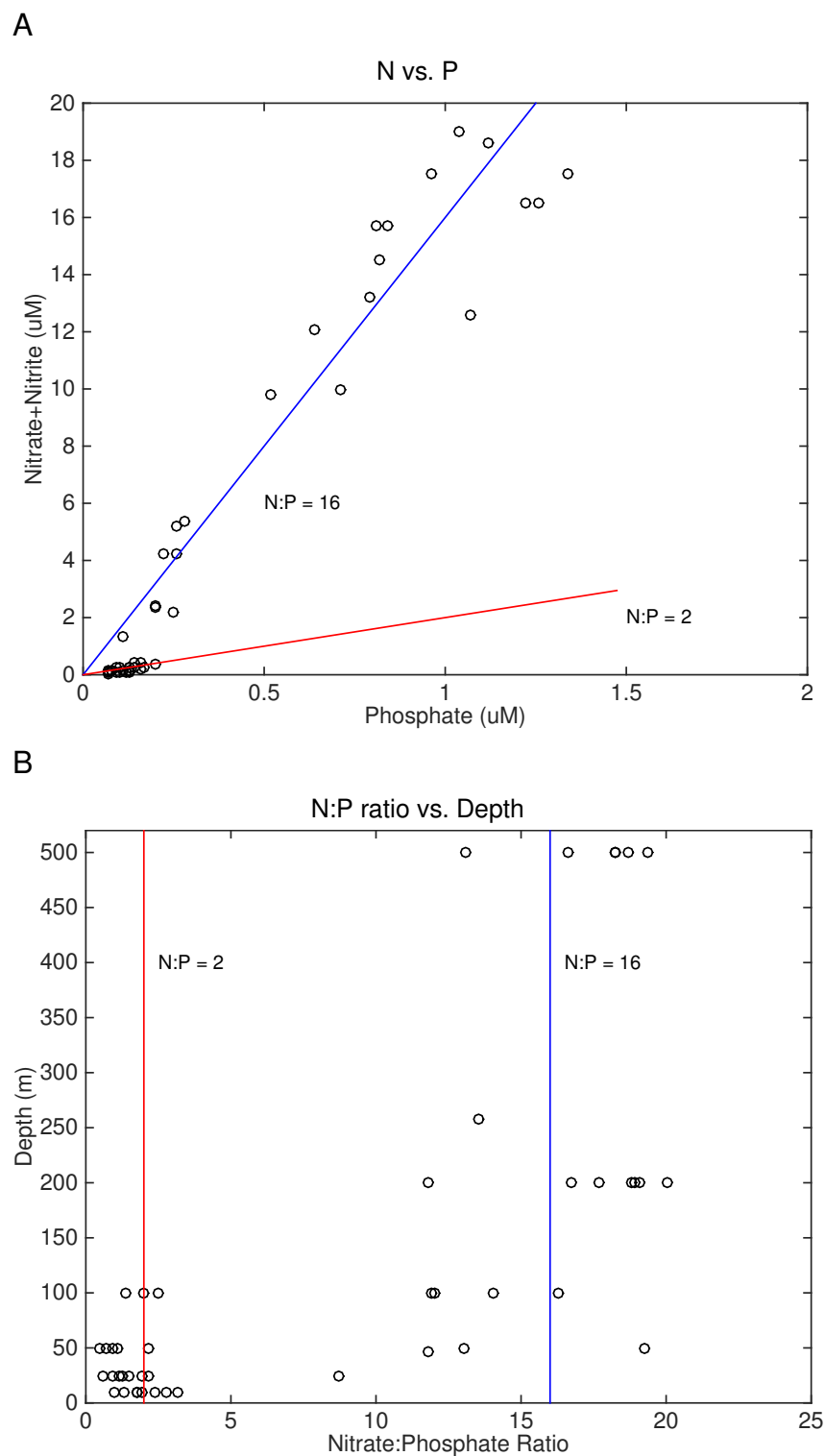


Figure S3. N:P ratio, calculated as nitrate+nitrite to phosphate ratio, across samples plotted as (A) nitrate+nitrite vs. phosphate and (B) depth vs. N:P ratio. Typical Redfield ratio of N:P = 16 is shown as well as the observed N:P = 2 in surface samples.

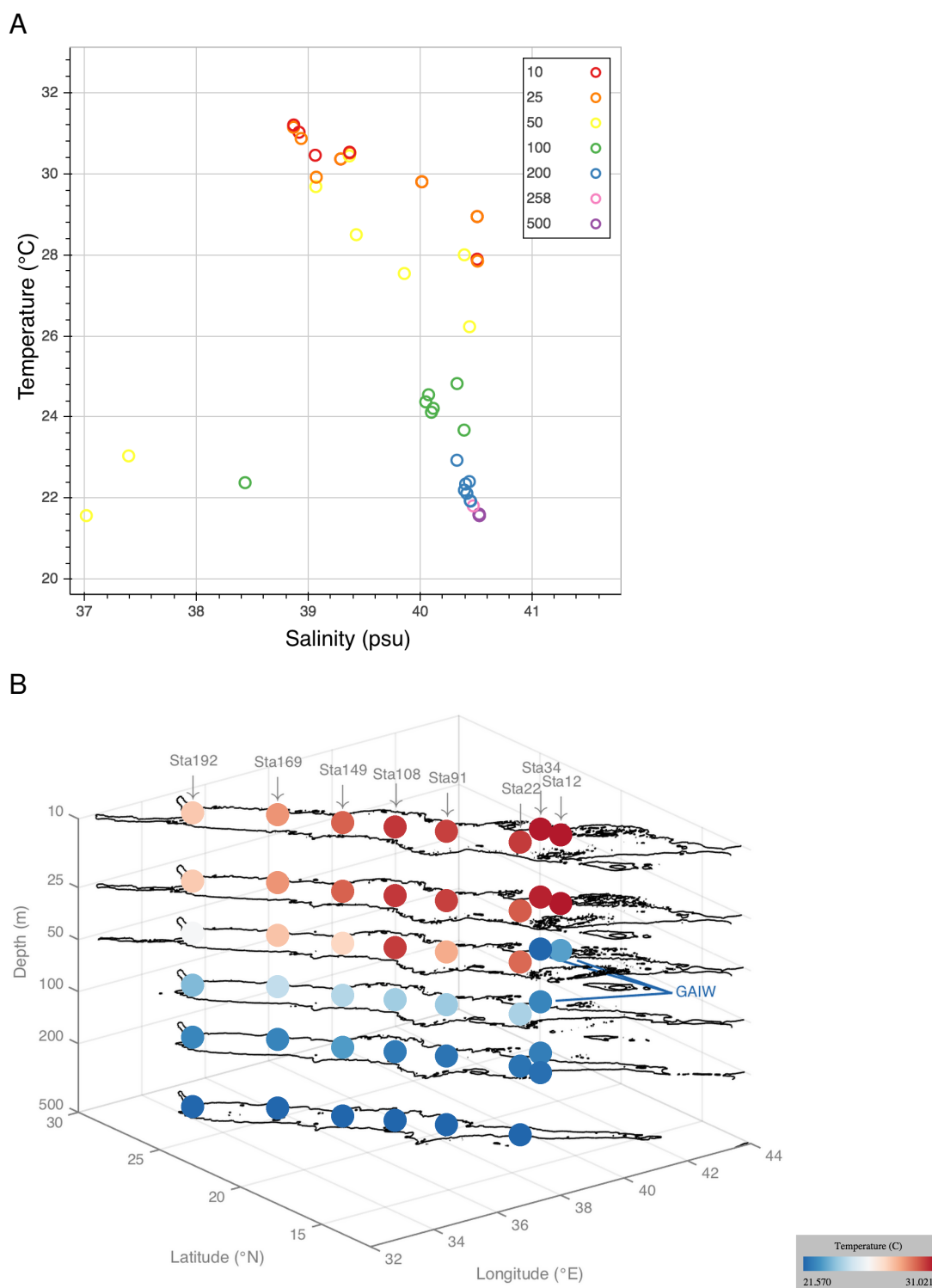


Figure S4. Temperature–salinity (T–S) relationship shown using publicly available interactive visualization tools. **(A)** T–S profile generated with Bokeh Python package and **(B)** 3D map of Red Sea colored by temperature generated with `ili Toolbox. Points shown are the 45 samples used in this study. The three GAIW foreign water mass samples are clearly visible as distinct from native Red Sea water mass samples by T–S profile and temperature anomaly in the water column.

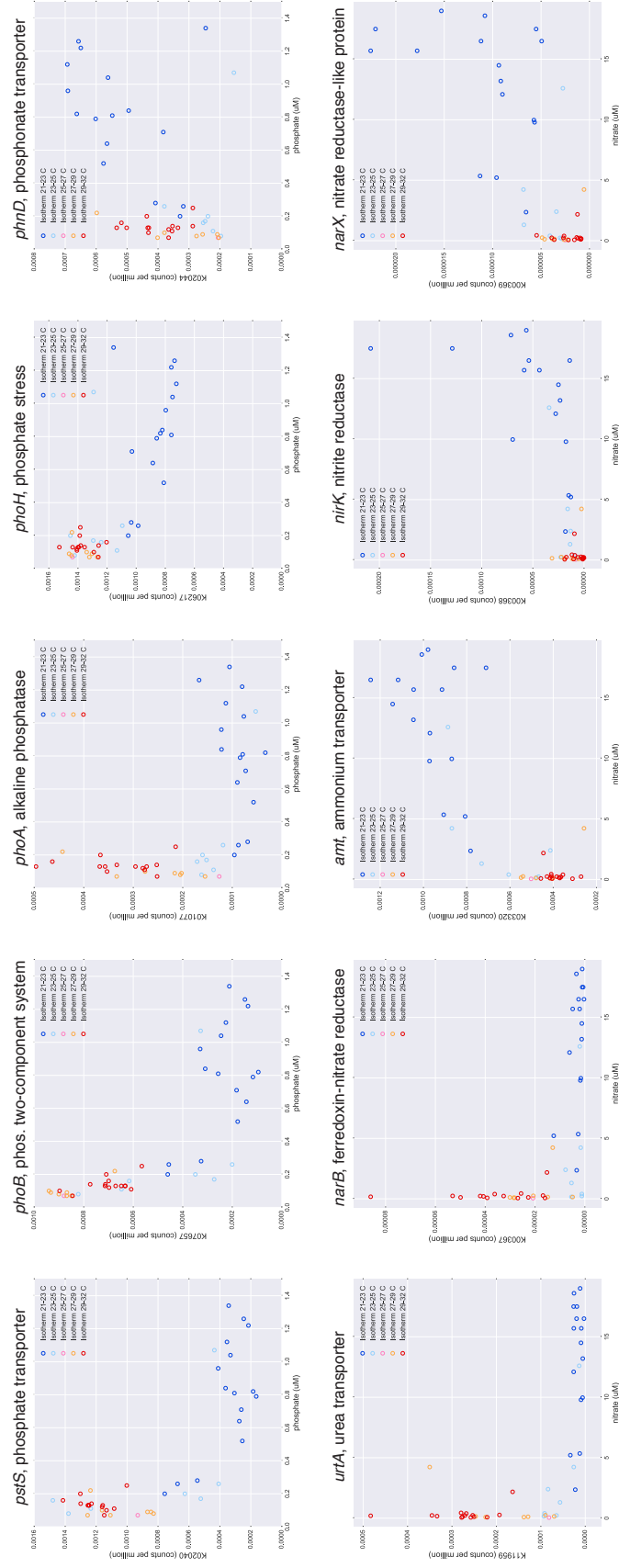


Figure S5. Covariation of nutrient acquisition KOs with phosphate and nitrate, separated by isotherms in 2-degree increments. KO relative abundance is given in units of counts per million of total KO counts in each sample (i.e., all KOs sum to 1 million in each sample).

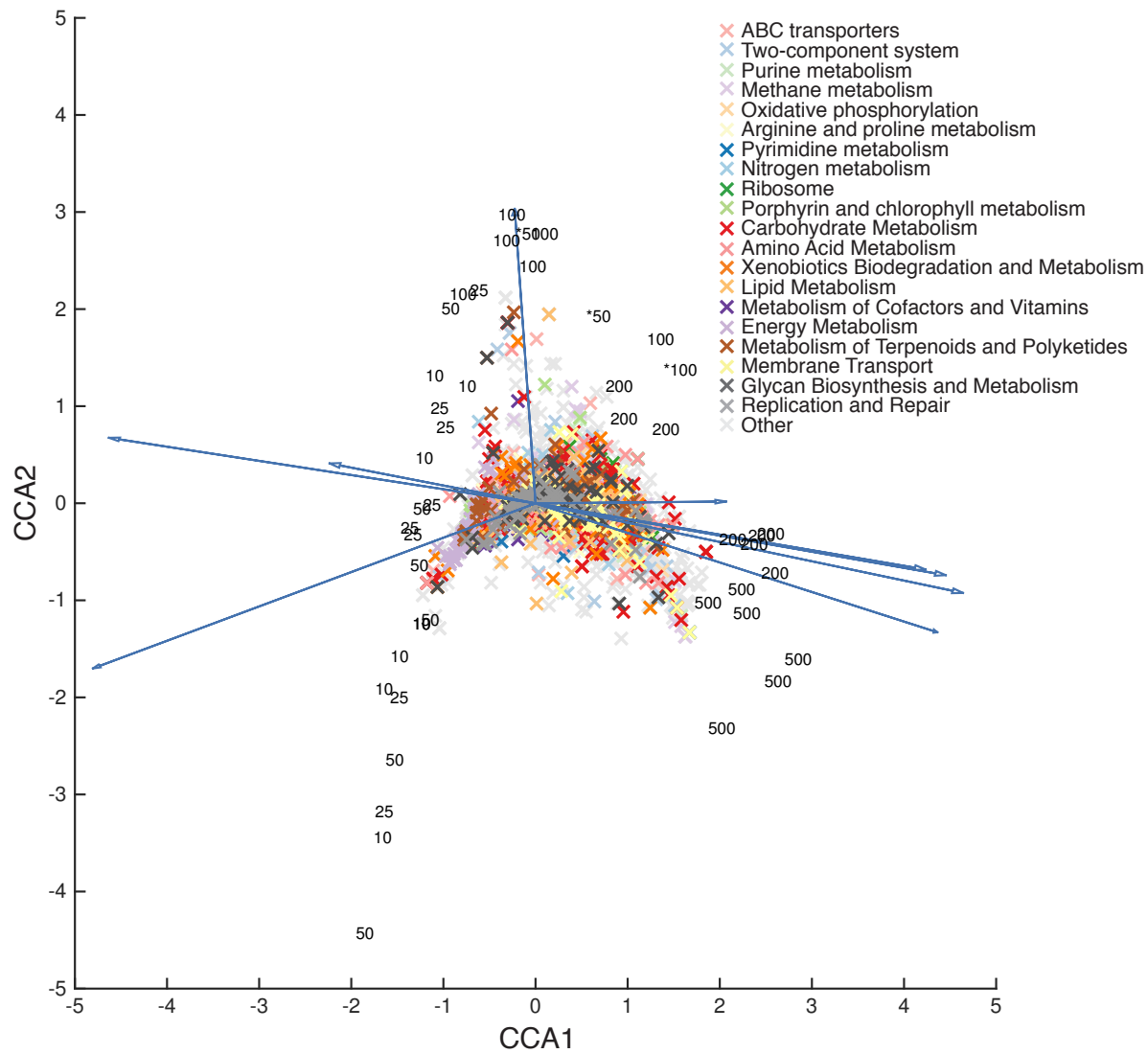


Figure S6. Canonical correspondence analysis of KO relative abundance with environmental parameters, with all KOs displayed. Samples are shown as black numerals indicating depth in meters (GAIW samples marked with asterisk), environmental parameters as dark blue arrows, and KOs colored by pathway.

Supplementary Tables

Table S1. Station properties. For each station, the following oceanographic features were calculated from CTD measurements: mixed layer depth (temperature decrease of 0.5 °C from surface), chlorophyll maximum, and oxygen minimum. Values of the chlorophyll maximum and oxygen minimum are given.

Station	Latitude (°N)	Longitude (°E)	Mixed layer (m)	Chlorophyll max. (m) (mg/m ³)	Oxygen min. (m) (mL/L)
12	17.662	40.905	31	44 (2.351)	n/a
22	17.996	39.799	57	63 (1.159)	311 (0.554)
34	18.580	40.743	40	48 (1.563)	n/a
91	20.525	38.781	35	83 (0.502)	278 (0.487)
108	22.046	37.929	53	97 (0.443)	381 (0.600)
149	23.604	37.054	52	99 (0.456)	465 (0.756)
169	25.772	36.116	47	97 (0.390)	546 (1.311)
192	27.897	34.507	40	58 (0.635)	498 (1.335)

Table S2. Sample water properties.

Sample	Station	Latitude (°N)	Longitude (°E)	Depth (m)	Temp. (°C)	Salinity (psu)	Oxygen (mL/L)	Chlorophyll (mg/m ³)	Turbidity (V)	Nitrate (μM)	Phosphate (μM)	Silicate (μM)
1				10	31.20	38.87	4.25	0.001	0.255	0.17	0.13	2.15
2	12	17.662	40.905	25	31.14	38.87	4.25	0.016	0.262	0.12	0.13	2.22
3				47	23.04	37.39	1.97	1.519	0.328	12.60	1.07	10.85
4				10	30.45	39.06	4.29	0.001	0.260	0.23	0.13	2.21
5				25	29.91	39.07	4.32	0.001	0.299	0.07	0.12	2.29
6	22	17.996	39.799	50	29.68	39.07	4.32	0.098	0.263	0.12	0.11	2.36
7				100	24.37	40.05	3.64	0.081	0.238	4.23	0.26	3.02
8				200	21.93	40.45	1.55	0.001	0.233	14.50	0.82	9.60
9				500	21.57	40.53	1.09	0.001	0.234	16.50	1.26	15.32
10				10	31.02	38.92	4.34	0.001	0.241	0.27	0.14	2.27
11				25	30.87	38.94	4.59	0.012	0.247	2.18	0.25	2.07
12	34	18.58	40.743	50	21.57	37.01	1.29	1.097	0.289	17.50	1.34	14.51
13				100	22.38	38.44	1.93	0.034	0.250	9.97	0.71	15.20
14				200	22.20	40.40	2.84	0.001	0.237	13.20	0.79	16.13
15				258	21.81	40.48	0.60	0.001	0.258	16.50	1.22	16.43
16				10	30.36	39.29	4.38	0.001	0.272	0.23	0.13	2.86
17				25	30.37	39.29	4.38	0.001	0.274	0.20	0.16	2.10
18	91	20.525	38.781	50	28.50	39.43	4.64	0.058	0.258	4.23	0.22	2.60
19				100	24.12	40.10	3.48	0.227	0.242	0.23	0.17	2.80
20				200	21.94	40.45	1.67	0.001	0.244	12.10	0.64	7.95
21				500	21.58	40.53	0.92	0.001	0.235	17.50	0.96	16.75
22				10	30.53	39.37	4.37	0.001	0.248	0.44	0.14	1.63
23				25	30.51	39.37	4.38	0.001	0.250	0.39	0.20	1.83
24	108	22.046	37.929	50	30.44	39.37	4.38	0.002	0.256	0.06	0.13	2.08
25				100	24.21	40.12	4.00	0.453	0.249	2.40	0.20	2.60
26				200	22.12	40.42	2.79	0.001	0.238	9.79	0.52	7.13
27				500	21.58	40.53	1.00	0.001	0.223	18.60	1.12	13.89
28				10	29.80	40.02	4.37	0.001	0.244	0.24	0.10	2.18
29				25	29.80	40.02	4.38	0.001	0.244	0.08	0.07	2.37
30	149	23.604	37.054	50	27.54	39.86	4.68	0.002	0.251	0.15	0.07	2.08
31				100	24.55	40.08	4.43	0.399	0.249	0.40	0.16	2.66
32				200	22.94	40.33	4.08	0.057	0.231	2.36	0.20	2.69
33				500	21.58	40.53	0.78	0.001	0.226	19.00	1.04	14.58
34				10	28.94	40.51	4.46	0.001	0.245	0.09	0.09	2.02
35				25	28.94	40.51	4.46	0.001	0.246	0.12	0.08	1.96
36	169	25.772	36.116	50	28.00	40.40	4.63	0.001	0.241	0.09	0.10	2.18
37				100	24.83	40.33	4.61	0.336	0.239	0.16	0.08	2.55
38				200	22.35	40.41	3.57	0.001	0.240	5.35	0.28	6.39
39				500	21.60	40.53	1.41	0.001	0.225	15.70	0.84	13.90
40				10	27.89	40.51	4.52	0.001	0.244	0.25	0.09	2.19
41				25	27.85	40.52	4.51	0.003	0.254	0.15	0.07	2.41
42	192	27.897	34.507	50	26.23	40.44	4.61	0.305	0.252	0.05	0.07	2.21
43				100	23.68	40.40	4.19	0.125	0.235	1.31	0.11	2.61
44				200	22.41	40.44	3.46	0.001	0.236	5.21	0.26	4.89
45				500	21.61	40.53	1.39	0.001	0.239	15.70	0.81	13.19

Table S3. Illumina metagenome properties. Number of reads and total size in bp of forward (Fwd) and reverse (Rev) sequenced reads are after PRINSEQ preprocessing.

Sample	Station	Insert size				Paired reads (M)	Total basepairs (Gbp)
		(median, bp)	(MAD, bp)	(mean, bp)	(SD, bp)		
1		299	118.6	311.6	130.8	9.6	1.8
2	12	305	118.6	315.5	129.7	13.5	2.5
3		284	120.1	294.2	128.1	11.5	2.1
4		204	106.7	215.0	102.7	9.9	1.8
5		270	115.6	278.7	121.6	7.7	1.4
6	22	274	120.1	282.9	124.8	7.7	1.4
7		279	117.1	288.7	124.6	8.8	1.6
8		273	117.1	282.0	122.8	8.0	1.5
9		356	129.0	367.8	140.6	8.1	1.5
10		316	121.6	324.9	131.7	13.5	2.5
11		302	124.5	311.4	132.8	11.5	2.1
12	34	286	124.5	292.1	126.8	9.9	1.8
13		230	111.2	237.8	108.0	7.7	1.4
14		258	117.1	264.3	117.0	7.7	1.4
15		283	124.5	288.3	126.7	8.8	1.6
16		359	133.4	373.3	145.7	15.7	2.9
17		366	134.9	380.1	147.9	8.1	1.5
18	91	244	134.9	252.5	124.8	8.0	1.5
19		186	106.7	198.8	98.4	11.5	2.1
20		183	102.3	194.8	93.8	9.9	1.8
21		233	117.1	239.4	111.2	11.3	2.1
22		353	129.0	362.4	139.8	11.7	2.2
23		273	123.1	279.2	123.6	10.5	2.0
24	108	203	102.3	211.6	97.6	11.6	2.2
25		284	126.0	289.8	126.7	9.6	1.8
26		274	127.5	279.4	125.9	11.1	2.1
27		277	124.5	283.6	125.8	10.5	2.0
28		315	129.0	322.8	135.8	11.5	2.1
29		357	136.4	369.0	146.8	9.6	1.8
30	149	316	129.0	325.6	136.0	11.7	2.2
31		339	129.0	352.6	139.7	8.0	1.5
32		219	103.8	228.6	104.2	11.6	2.2
33		245	115.6	252.6	114.2	9.6	1.8
34		328	126.0	337.4	136.3	13.5	2.5
35		284	121.6	295.1	129.6	10.5	2.0
36	169	305	123.1	313.1	129.2	13.9	2.6
37		227	109.7	237.8	109.5	11.3	2.1
38		245	120.1	252.4	115.6	13.5	2.5
39		188	100.8	199.4	95.3	8.8	1.6
40		324	124.5	334.2	133.5	15.7	2.9
41		348	126.0	357.4	136.9	8.1	1.5
42	192	337	127.5	344.9	136.7	13.5	2.5
43		364	132.0	372.1	141.7	10.9	2.0
44		267	121.6	273.5	120.6	11.5	2.1
45		259	115.6	266.8	117.3	11.3	2.1
	Max:	366		380.1		Total: 477.7	88.8
	Min:	183		194.8			
	Mean:	282.7		291.9			

Table S4. Parameters used in PRINSEQ preprocessing, listed in the order that processing steps were applied.

Parameter	Value	Description
trim_qual_left	20	Trim sequence from 5'-end with quality threshold of 20
trim_qual_right	20	Trim sequence from 3'-end with quality threshold of 20
trim_ns_left	1	Trim poly-N tail from 5'-end
trim_ns_right	1	Trim poly-N tail from 3'-end
min_len	40	Filter sequences shorter than 40 bp (after trimming)
min_qual_mean	20	Filter sequences with mean quality threshold of 20 (after trimming)
ns_max_p	5	Filter sequences with more than 5% Ns (after trimming)
lc_method	entropy	Filter low complexity sequences with Shannon entropy. . .
lc_threshold	50	. . . less than 50 (after trimming)
derep	14	Filter exact duplicates and reverse complement exact duplicates (after trimming)

Table S5. Results of AICc, the stepwise explanation of variation in response variables by sequentially adding environmental parameters (predictors), balancing performance and parsimony.

File: Table_S5_AICc_Results.xlsx

Table S6. Percent of all forward reads mapped by HUMAnN and taxonomy assignment methods. Columns from left to right: HUMAnN translated search to prokaryotic KO sequences in KEGG; CLARK genus-level k-mer; CLARK species-level k-mer; Kraken genus-level k-mer; GraftM genus-level 16S; GraftM ecotype-level *Prochlorococcus rpoC1*; GraftM ecotype-level *Pelagibacter* 16S.

File: Table_S6_Percent_Reads_Mapped.xlsx

Table S7. KOs ranked by total abundance across all samples.

File: Table_S7_KOs_Ranked_By_Abundance.xlsx

Table S8. KOs clustered by total abundance across all samples using partitioning around medoids (PAM) with 12 clusters.

File: Table_S8_KOs_Partitioned_Around_Medoids.xlsx

Table S9. Cartesian and polar coordinates of the 224 KEGG KOs (gene ortholog groups) plotted in the CCA ordination. KOs were first assigned to second-tier KEGG pathways (if total pathway count was at least 5), then first-tier KEGG pathways (if total pathway count was at least 5), and the remaining KOs were grouped as ‘Other’. Direction is in degrees from the polar axis. For reference, environmental parameter directions are as follows: salinity, 0.5°; chlorophyll, 94.3°; turbidity, 169.6°; oxygen, 171.7°; temperature, -160.5°; depth, -16.9°; nitrate, -11.2°; silicate, -9.4°; phosphate, -9.1°.

KO number	Description	CCA1	CCA2	Direction (°)	Magnitude
Oxidative phosphorylation (2nd tier)					
K00239	succinate dehydrogenase flavoprotein subunit	0.205	0.789	75.4	0.815
K00240	succinate dehydrogenase iron-sulfur protein	0.092	0.763	83.1	0.768
K00330	NADH dehydrogenase I subunit A	0.360	0.342	43.5	0.496
K00331	NADH dehydrogenase I subunit B	0.400	0.593	56.0	0.715
K00333	NADH dehydrogenase I subunit D	0.398	0.589	55.9	0.711
K00335	NADH dehydrogenase I subunit F	-0.069	1.182	93.3	1.184
K00338	NADH dehydrogenase I subunit I	0.371	0.549	56.0	0.662
K00340	NADH dehydrogenase I subunit K	0.518	0.293	29.5	0.595
K00341	NADH dehydrogenase I subunit L	0.479	0.413	40.7	0.633
K00342	NADH dehydrogenase I subunit M	0.492	0.462	43.2	0.675
K00356	NADH dehydrogenase	-0.991	0.583	149.5	1.150
K00411	ubiquinol-cytochrome c reductase iron-sulfur subunit	0.356	0.184	27.3	0.400
K00412	ubiquinol-cytochrome c reductase cytochrome b subunit	-0.526	0.702	126.9	0.877
K02108	F-type H ⁺ -transporting ATPase subunit a	-0.573	0.277	154.2	0.636
K02109	F-type H ⁺ -transporting ATPase subunit b	-1.208	-0.926	-142.5	1.522
K02111	F-type H ⁺ -transporting ATPase subunit alpha	-0.390	0.582	123.9	0.701
K02112	F-type H ⁺ -transporting ATPase subunit beta	-0.325	0.614	117.9	0.695
K02117	V-type H ⁺ -transporting ATPase subunit A	2.886	-0.036	-0.7	2.886
K02118	V-type H ⁺ -transporting ATPase subunit B	2.902	-0.242	-4.8	2.912
K02258	cytochrome c oxidase subunit XI assembly protein	-1.499	-0.941	-147.9	1.770
K02276	cytochrome c oxidase subunit III	-0.538	0.098	169.7	0.547
K02301	protoheme IX farnesyltransferase	0.373	-0.578	-57.2	0.688
K05575	NADH dehydrogenase I subunit 4	-2.203	-3.947	-119.2	4.520
ABC transporters (2nd tier)					
K01997	branched-chain amino acid transport system permease protein	-0.134	0.556	103.6	0.571
K02000	glycine betaine/proline transport system ATP-binding protein	0.381	1.484	75.6	1.533
K02001	glycine betaine/proline transport system permease protein	0.290	1.557	79.4	1.584
K02002	glycine betaine/proline transport system substrate-binding protein	0.311	1.409	77.5	1.443
K02006	cobalt/nickel transport system ATP-binding protein	-1.884	-3.807	-116.3	4.248
K02031	peptide/nickel transport system ATP-binding protein	0.432	-0.276	-32.6	0.512
K02032	peptide/nickel transport system ATP-binding protein	0.462	-0.170	-20.2	0.492
K02033	peptide/nickel transport system permease protein	0.368	-0.290	-38.2	0.468
K02036	phosphate transport system ATP-binding protein	-1.317	-0.051	-177.8	1.318
K02037	phosphate transport system permease protein	-1.382	-0.692	-153.4	1.545
K02038	phosphate transport system permease protein	-1.409	-0.807	-150.2	1.624
K02040	phosphate transport system substrate-binding protein	-1.382	-0.708	-152.9	1.553
K02049	sulfonate/nitrate/taurine transport system ATP-binding protein	0.504	0.155	17.1	0.528
K02050	sulfonate/nitrate/taurine transport system permease protein	0.550	-0.165	-16.7	0.574
K09686	antibiotic transport system permease protein	0.703	-1.528	-65.3	1.682
Pyrimidine metabolism (2nd tier)					
K00384	thioredoxin reductase (NADPH)	-0.263	0.292	132.0	0.393
K00525	ribonucleoside-diphosphate reductase alpha chain	0.105	0.841	82.9	0.848
K00526	ribonucleoside-diphosphate reductase beta chain	-0.341	1.203	105.8	1.250
K00962	polyribonucleotide nucleotidyltransferase	-0.501	0.447	138.3	0.672
K01464	dihydropyrimidinase	2.122	-1.029	-25.9	2.359
K01465	dihydroorotase	-0.551	0.510	137.2	0.751
K01485	cytosine deaminase	-1.261	-3.239	-111.3	3.476
K01493	dCMP deaminase	2.173	0.206	5.4	2.182
K02338	DNA polymerase III subunit beta	-1.004	-0.198	-168.9	1.023
K03040	DNA-directed RNA polymerase subunit alpha	-0.513	0.398	142.2	0.649
K03043	DNA-directed RNA polymerase subunit beta	-0.412	0.588	125.0	0.718
K03046	DNA-directed RNA polymerase subunit beta'	-0.536	0.338	147.8	0.634
K03465	thymidylate synthase (FAD)	-0.610	0.845	125.8	1.042

Table S9. (continued)

KO number	Description	CCA1	CCA2	Direction (°)	Magnitude
Carbon fixation pathways in prokaryotes (2nd tier)					
K00174	2-oxoglutarate ferredoxin oxidoreductase subunit alpha	1.521	0.848	29.2	1.741
K00175	2-oxoglutarate ferredoxin oxidoreductase subunit beta	1.795	0.497	15.5	1.863
K00626	acetyl-CoA C-acetyltransferase	0.714	0.261	20.0	0.760
K01681	aconitate hydratase I	0.455	0.733	58.2	0.863
K01848	methylmalonyl-CoA mutase, N-terminal domain	2.450	0.061	1.4	2.451
K01849	methylmalonyl-CoA mutase, C-terminal domain	2.754	-0.562	-11.5	2.811
K01902	succinyl-CoA synthetase alpha subunit	0.290	0.718	68.0	0.774
K01903	succinyl-CoA synthetase beta subunit	0.299	0.750	68.3	0.807
K01963	acetyl-CoA carboxylase carboxyl transferase subunit beta	-0.774	-0.025	-178.2	0.774
K01966	propionyl-CoA carboxylase beta chain	1.321	0.351	14.9	1.367
Glycine, serine and threonine metabolism (2nd tier)					
K00302	sarcosine oxidase, subunit alpha	-0.279	1.160	103.5	1.193
K00303	sarcosine oxidase, subunit beta	-0.186	1.070	99.8	1.086
K00304	sarcosine oxidase, subunit delta	-0.364	1.131	107.9	1.188
K00315	dimethylglycine dehydrogenase	0.124	1.044	83.2	1.051
K00544	betaine-homocysteine S-methyltransferase	1.849	1.960	46.7	2.695
K00600	glycine hydroxymethyltransferase	0.237	-0.011	-2.6	0.237
K00605	aminomethyltransferase	-0.174	0.681	104.3	0.703
K00613	glycine amidinotransferase	-0.638	2.037	107.4	2.135
K01079	phosphoserine phosphatase	2.331	-0.773	-18.3	2.456
K01733	threonine synthase	0.928	-0.708	-37.3	1.168
Ribosome (2nd tier)					
K02867	large subunit ribosomal protein L11	0.243	0.217	41.7	0.326
K02877	large subunit ribosomal protein L15e	3.098	-1.077	-19.2	3.280
K02884	large subunit ribosomal protein L19	-0.394	0.571	124.6	0.694
K02899	large subunit ribosomal protein L27	-0.353	0.593	120.8	0.690
K02929	large subunit ribosomal protein L44e	3.112	-1.281	-22.4	3.365
K02945	small subunit ribosomal protein S1	-0.859	-0.516	-149.0	1.002
K02946	small subunit ribosomal protein S10	0.068	0.483	82.0	0.488
K02950	small subunit ribosomal protein S12	0.132	0.384	71.0	0.406
K02959	small subunit ribosomal protein S16	-0.620	0.343	151.1	0.708
Porphyrin and chlorophyll metabolism (2nd tier)					
K00218	protochlorophyllide reductase	-2.262	-4.865	-114.9	5.365
K00228	coproporphyrinogen III oxidase	-0.788	-0.250	-162.4	0.826
K00798	cob(II)alamin adenosyltransferase	-0.489	-2.775	-100.0	2.818
K01772	ferrochelatase	-0.745	-0.419	-150.7	0.855
K01845	glutamate-1-semialdehyde 2,1-aminomutase	1.173	-0.982	-39.9	1.530
K03394	cobalt-factor-2 C20-methyltransferase	1.405	-2.693	-62.4	3.038
K05934	precorrin-3B C17-methyltransferase	3.089	-1.324	-23.2	3.361
K09882	cobaltochelatase CobS	-0.571	0.732	128.0	0.929

Table S9. (continued)

KO number	Description	CCA1	CCA2	Direction (°)	Magnitude
Amino acid metabolism					
K00249	acyl-CoA dehydrogenase	0.144	1.025	82.0	1.035
K00797	spermidine synthase	-0.963	-0.588	-148.6	1.128
K00826	branched-chain amino acid aminotransferase	0.397	-0.269	-34.2	0.480
K00930	acetylglutamate kinase	0.795	-0.966	-50.6	1.251
K01251	adenosylhomocysteinase	0.118	0.290	67.8	0.313
K01480	agmatinase	0.005	0.160	88.1	0.161
K01649	2-isopropylmalate synthase	0.154	0.252	58.5	0.295
K01652	acetolactate synthase I/II/III large subunit	0.263	0.232	41.5	0.350
K01692	enoyl-CoA hydratase	0.411	0.752	61.4	0.857
K01714	dihydrodipicolinate synthase	-0.464	0.227	153.9	0.517
K01739	cystathionine gamma-synthase	-1.380	-2.856	-115.8	3.172
K01740	O-acetylhomoserine (thiol)-lyase	-0.305	0.605	116.8	0.677
K01814	phosphoribosylformimino-5-aminoimidazole carboxamide ribotide	-0.768	0.073	174.6	0.771
K01915	glutamine synthetase	0.242	0.670	70.2	0.712
K02502	ATP phosphoribosyltransferase regulatory subunit	-1.307	-1.461	-131.8	1.961
K05710	ferredoxin subunit of phenylpropionate dioxygenase	2.715	-1.362	-26.6	3.038
K08963	methylthioribose-1-phosphate isomerase	1.133	0.028	1.4	1.133
Carbohydrate metabolism					
K00074	3-hydroxybutyryl-CoA dehydrogenase	1.347	0.592	23.7	1.471
K00101	L-lactate dehydrogenase (cytochrome)	-0.890	1.500	120.7	1.744
K00615	transketolase	0.326	-0.113	-19.1	0.345
K00965	UDPglucose-hexose-1-phosphate uridylyltransferase	2.973	-1.502	-26.8	3.330
K01006	pyruvate,orthophosphate dikinase	0.402	0.452	48.4	0.605
K01610	phosphoenolpyruvate carboxykinase (ATP)	1.593	-0.193	-6.9	1.605
K01644	citrate lyase subunit beta	1.984	-0.538	-15.2	2.056
K01708	galactarate dehydratase	-1.036	1.426	126.0	1.763
K01711	GDPmannose 4,6-dehydratase	0.164	0.510	72.2	0.536
K01858	myo-inositol-1-phosphate synthase	2.431	-1.072	-23.8	2.657
K03821	polyhydroxyalkanoate synthase	2.471	-2.366	-43.8	3.421
Energy metabolism (1st tier)					
K00381	sulfite reductase (NADPH) hemoprotein beta-component	2.424	-0.970	-21.8	2.611
K00958	sulfate adenyltransferase	1.306	-1.626	-51.2	2.085
K02639	ferredoxin	-2.082	-2.329	-131.8	3.124
K02703	photosystem II PsbA protein	-1.499	3.524	113.0	3.830
K03518	carbon-monoxide dehydrogenase small subunit	1.250	0.716	29.8	1.440
K04748	nitric-oxide reductase NorQ protein	3.052	-1.345	-23.8	3.336
K11212	LPPG:FO 2-phospho-L-lactate transferase	2.966	-1.351	-24.5	3.259
Metabolism of cofactors and vitamins (1st tier)					
K00324	NAD(P) transhydrogenase subunit alpha	-0.537	0.187	160.8	0.568
K01633	dihydroneopterin aldolase	-1.114	-0.261	-166.8	1.144
K01737	6-pyruvoyl tetrahydrobiopterin synthase	-1.159	-2.190	-117.9	2.478
K03147	thiamine biosynthesis protein ThiC	1.168	-1.640	-54.6	2.013
K03182	3-octaprenyl-4-hydroxybenzoate carboxy-lyase UbiD	2.841	-0.816	-16.0	2.956
K03186	3-octaprenyl-4-hydroxybenzoate carboxy-lyase UbiX	2.708	-0.400	-8.4	2.737
K03644	lipic acid synthetase	-0.657	-0.228	-160.9	0.696
K06215	pyridoxine biosynthesis protein	2.013	0.032	0.9	2.013
Metabolism of terpenoids and polyketides (1st tier)					
K00973	glucose-1-phosphate thymidyltransferase	0.851	0.114	7.7	0.859
K01662	1-deoxy-D-xylulose-5-phosphate synthase	-0.630	0.003	179.7	0.630
K01710	dTDP-glucose 4,6-dehydratase	0.609	0.060	5.6	0.612
K06443	lycopene beta cyclase	-1.837	-0.982	-151.9	2.083
K10027	phytoene dehydrogenase	-1.585	1.257	141.6	2.023
Folding, sorting and degradation (1st tier)					
K00970	poly(A) polymerase	-1.192	-2.531	-115.2	2.797
K03100	signal peptidase I	-0.821	-0.851	-134.0	1.182
K03432	proteasome alpha subunit	3.028	-1.127	-20.4	3.231
K03433	proteasome beta subunit	3.191	-1.299	-22.2	3.446
K03628	transcription termination factor Rho	-0.172	0.972	100.0	0.987
K04077	chaperonin GroEL	-0.389	0.302	142.2	0.493
Translation (1st tier)					
K01876	aspartyl-tRNA synthetase	0.301	-0.142	-25.2	0.333
K01880	glycyl-tRNA synthetase	1.380	0.230	9.4	1.399
K03231	elongation factor EF-1 alpha subunit	3.121	-1.299	-22.6	3.381
K03242	translation initiation factor eIF-2 gamma subunit	3.160	-1.168	-20.3	3.369
K03243	translation initiation factor IF-2 unclassified subunit	3.306	-1.719	-27.5	3.726

Table S9 (continued)

KO number	Description	CCA1	CCA2	Direction (°)	Magnitude
Other					
K00208	enoyl-[acyl-carrier protein] reductase I	-0.544	0.448	140.5	0.705
K00528	ferredoxin-NADP+ reductase	1.931	0.470	13.7	1.987
K00574	cyclopropane-fatty-acyl-phospholipid synthase	-0.452	0.852	118.0	0.964
K00666	fatty-acyl-CoA synthase	0.107	1.027	84.1	1.033
K00799	glutathione S-transferase	-0.683	-1.314	-117.5	1.481
K00809	deoxyhypusine synthase	0.804	0.011	0.8	0.804
K00986	RNA-directed DNA polymerase	3.061	-5.265	-59.8	6.090
K01247	DNA-3-methyladenine glycosylase II	-1.242	0.706	150.4	1.429
K01256	aminopeptidase N	-1.110	-2.954	-110.6	3.155
K01271	X-Pro dipeptidase	0.563	1.057	62.0	1.198
K01358	ATP-dependent Clp protease, protease subunit	-0.723	-0.529	-143.8	0.896
K01488	adenosine deaminase	1.769	1.211	34.4	2.143
K01669	deoxyribodipyrimidine photo-lyase	-1.796	-2.189	-129.4	2.831
K01919	glutamate-cysteine ligase	-1.189	-1.702	-124.9	2.076
K01920	glutathione synthase	-1.207	-1.630	-126.5	2.028
K01971	DNA ligase (ATP)	-1.360	-3.437	-111.6	3.696
K01972	DNA ligase (NAD+)	-0.884	-1.491	-120.7	1.734
K02005	HlyD family secretion protein	-2.047	-4.479	-114.6	4.925
K02014	iron complex outermembrane receptor protein	0.946	-0.275	-16.2	0.986
K02025	multiple sugar transport system permease protein	-0.535	0.331	148.2	0.629
K02026	multiple sugar transport system permease protein	-0.516	0.184	160.4	0.548
K02027	multiple sugar transport system substrate-binding protein	-0.795	-0.078	-174.4	0.798
K02057	simple sugar transport system permease protein	-0.537	0.442	140.5	0.695
K02116	ATP synthase protein I	-1.334	-1.060	-141.5	1.704
K02221	YggT family protein	-0.866	0.045	177.0	0.867
K02313	chromosomal replication initiator protein DnaA	-0.665	0.221	161.7	0.701
K02355	elongation factor EF-G	-0.242	0.733	108.3	0.772
K02358	elongation factor EF-Tu	-0.140	0.556	104.1	0.573
K02469	DNA gyrase subunit A	-0.587	-0.158	-164.9	0.608
K02520	translation initiation factor IF-3	-0.516	0.339	146.7	0.617
K03086	RNA polymerase primary sigma factor	-0.771	-0.498	-147.1	0.918
K03088	RNA polymerase sigma-70 factor, ECF subfamily	0.683	-0.075	-6.3	0.687
K03124	transcription initiation factor TFIIB	3.227	-1.393	-23.3	3.514
K03166	DNA topoisomerase VI subunit A	3.148	-1.169	-20.4	3.358
K03167	DNA topoisomerase VI subunit B	3.374	-2.041	-31.2	3.943
K03234	elongation factor EF-2	3.102	-0.937	-16.8	3.240
K03320	ammonium transporter, Amt family	1.107	0.068	3.5	1.109
K03406	methyl-accepting chemotaxis protein	1.923	-2.502	-52.4	3.156
K03455	monovalent cation:H+ antiporter-2, CPA2 family	2.557	-1.067	-22.7	2.770
K03495	glucose inhibited division protein A	-0.613	-0.109	-169.9	0.623
K03502	DNA polymerase V	-1.054	-0.051	-177.2	1.056
K03564	peroxiredoxin Q/BCP	-0.394	-1.461	-105.1	1.513
K03568	TldD protein	-1.140	-0.975	-139.5	1.500
K03569	rod shape-determining protein MreB and related proteins	-0.424	0.442	133.8	0.612
K03592	PmbA protein	-1.631	-2.532	-122.8	3.012
K03596	GTP-binding protein LepA	-0.393	0.449	131.2	0.596
K03671	thioredoxin I	0.333	0.195	30.4	0.386
K03684	ribonuclease D	-1.182	-0.895	-142.9	1.483
K03702	excinuclease ABC subunit B	-0.344	0.730	115.3	0.807
K03704	cold shock protein (beta-ribbon, CspA family)	0.294	0.151	27.2	0.330
K03709	DtxR family transcriptional regulator, Mn-dependent transcriptional	3.055	-1.756	-29.9	3.523
K03711	Fur family transcriptional regulator, ferric uptake regulator	-0.755	-0.384	-153.0	0.847
K03718	Lrp/AsnC family transcriptional regulator, regulator for asnA, asnC	2.967	-1.757	-30.6	3.449
K03742	competence/damage-inducible protein ClnA	-1.036	-0.396	-159.1	1.109
K03768	peptidyl-prolyl cis-trans isomerase B (cyclophilin B)	0.753	-0.391	-27.5	0.849
K03797	carboxyl-terminal processing protease	-0.860	-0.759	-138.6	1.147
K03798	cell division protease FtsH	-0.769	-0.734	-136.3	1.063
K03924	MoxR-like ATPase	1.119	1.649	55.8	1.993
K04069	pyruvate formate lyase activating enzyme	3.438	-3.072	-41.8	4.611
K04483	DNA repair protein RadA	3.148	-1.359	-23.3	3.429
K04488	nitrogen fixation protein NifU and related proteins	0.474	0.988	64.4	1.096
K06147	ATP-binding cassette, subfamily B, bacterial	-0.868	-1.876	-114.8	2.067
K06174	ATP-binding cassette, sub-family E, member 1	3.230	-1.268	-21.4	3.470
K06188	aquaporin Z	2.989	-1.125	-20.6	3.194
K06206	sugar fermentation stimulation protein A	-1.300	-1.108	-139.6	1.708
K06207	GTP-binding protein	-1.243	-0.953	-142.5	1.566
K06213	magnesium transporter	-0.783	-0.076	-174.4	0.787
K06217	phosphate starvation-inducible protein PhoH and related proteins	-0.648	0.124	169.2	0.660
K06920	queuosine biosynthesis protein QueC	1.108	-1.680	-56.6	2.012
K07319	putative adenine-specific DNA-methyltransferase	1.545	0.115	4.3	1.550
K07442	tRNA (adenine-N1-)-methyltransferase	3.074	-1.412	-24.7	3.383
K07483	transposase	2.147	-2.464	-48.9	3.268
K07493	putative transposase	1.206	-0.320	-14.9	1.248
K07497	putative transposase	1.306	-0.409	-17.4	1.369
K07657	two-component system, OmpR family, phosphate regulon response	-1.322	-0.348	-165.2	1.367
K07738	transcriptional repressor NrdR	-0.678	0.115	170.4	0.688
K09014	Fe-S cluster assembly protein SufB	0.385	0.082	12.0	0.393